

# Physics informed neural network for forward and inverse radiation heat transfer in graded-index medium.

K. Murari \*      S. Sundar \*

December 20, 2024

\*Centre for Computational Mathematics and Data Science  
Department of Mathematics, IIT Madras, Chennai 600036, India  
kmurari2712@gmail.com, slnt@iitm.ac.in

## Abstract

Radiation heat transfer in a graded-index medium often suffers accuracy problems due to the gradual changes in the refractive index. The finite element method, meshfree, and other numerical methods often struggle to maintain accuracy when applied to this medium. To address this issue, we apply physics-informed neural networks (PINNs)-based machine learning algorithms to simulate forward and inverse problems for this medium. We also provide the theoretical upper bounds. This theoretical framework is validated through numerical experiments of predefined and newly developed models that demonstrate the accuracy and robustness of the algorithms in solving radiation transport problems in the medium. The simulations show that the novel algorithm goes on with numerical stability and effectively mitigates oscillatory errors, even in cases with more pronounced variations in the refractive index.

**Keywords:** Radiation transfer, Graded-index, Forward Problems, Inverse Problems, Total Error.

## 1 Introduction

Radiation heat transfer in graded index materials involves the transmission of thermal energy through electromagnetic waves within a material exhibiting varying refractive index. Typically, this index changes gradually from the center to the material's surface, impacting radiation propagation and heat transfer mechanisms. Understanding the complexities of heat transfer in the materials is paramount. Unlike homogeneous materials, which maintain a constant refractive index, graded index materials undergo gradual changes, significantly affecting thermal radiation propagation. This study delves into how these variations in refractive index impact the accuracy and stability of radiation heat transfer models, which are crucial for optimizing diverse heat transfer processes in materials engineering and thermal management applications. The pivotal role of radiation across various applications justifies this focus, ranging from interpreting spectroscopic emissions in celestial bodies [16], nuclear engineering [23], biological tissues [36], thermal insulation [3], gas turbines [38], combustion systems [12] and radiotherapy dose simulation [34]. Many researchers are actively working on this topic, and the radiative transfer community has focused on analyzing the complexities of radiation heat transmission through such media. Monte Carlo Method [44], Least-Square Finite Element Method(LSFEM) [26], Discontinuous Finite Element Method(DFEM) [14], Finite Volume Method(FVM) [24], Petrov–Galerkin Method(MLPG) [25], Least-Squares Spectral Element Method(LSSEM) [50], Spectral Element Method(SEM, LSSEM, and meshless method) [42] have simulated these types problems. Traditional methods like the LSFEM, the Galerkin Finite Element Method(GFEM) [50], and specific meshfree methods [51] suffer from various deficiencies. These methods have apparent shortcomings: First, the results show noticeable unwanted fluctuations (high-frequency errors). While the outcomes generally correspond well with the precise solutions, notable disparities still exist. Lattice Boltzmann method(LBM) [27], [47], Multi-Relaxation Time (MRT) Lattice Boltzmann method [15], and generalized lattice Boltzmann method [48] have also been to simulate the models.

## Nomenclature

$c_o$	speed of light	$\sigma$	activation function
$n$	refractive index	$T$	temperature distribution [K]
$s$	position vector	$\mathbf{1}_{[.]}$	unit step function
$k_e$	extinction coefficient	$\rho$	diffuse reflectivity
$\Omega$	direction vector	$\varepsilon_{\bar{\omega}}$	emissivity
$\Phi$	scattering phase function	$\Theta$	dimensionless temperature
$k_a$	absorption coefficient	$L$	length
$k_s$	scattering coefficient	$\mu$	directional cosine
$T_g$	medium temperature [K]	$\rho_m$	material density
$\Omega'$	incoming direction	$\sigma_B$	Stefan-Boltzmann constant
$\hat{n}_\omega$	normal vector to surface	$I_c$	collimated intensity from laser
$\Omega_{rs}$	incident direction of specular reflection	$I_d$	diffuse intensity
$I_{bw}$	black body intensity	$\omega$	scattering albedo
$I$	radiative intensity	$b$	black-body state
$S$	source term of differential equation	$0, L$	left and right boundaries
$G(s, t)$	incident radiation	$\mathbf{i}, \mathbf{j}, \mathbf{k}$	unit vectors
$q(s, t)$	heat flux [ $\text{W m}^{-2}$ ]	$\lambda$	learning rate
$\rho^{spce}$	specular reflectivity	$\lambda_{reg}$	regularization parameters
$K - 1$	number of hidden layers	$\Omega$	outgoing direction
$n_\theta$	number of times model retrained in parallel	$\tanh$	hyperbolic tangent( activation function)
$N_{int}$	number of interior points	$N_{sb}$	number of Sobol points
$N_{tb}$	number of temporal points	$N_d$	number of data points
$N$	number of collocations or training points		

Deep learning is an alternative way to avoid the curse of dimensionality. Due to this reason, deep learning has recently been an essential tool in modern technology and advanced research in the last few years. This learning contains many layers of transformations and scalar nonlinearities. Deep learning techniques demonstrate strong capabilities in approximating highly nonlinear functions. Their computational framework, which employs statistical learning and large-scale optimization methods in conjunction with contemporary hardware and software, enhances their capacity to address nonlinear and high-dimensional partial differential equations (PDEs). Deep neural networks (DNNs) are well known for their ability to universally approximate functions. This property holds under certain conditions, as demonstrated in research by Cybenko [7], Hornik et al. [18], [4], and Yarotsky [46]. This property makes them well-suited as trial functions for solving PDEs. A standard method involves minimizing the residual of the PDE by evaluating it at selected points within the domain, often called collocation points. Researchers have developed several deep-learning algorithms. PINNs [35] a meshfree deep learning algorithms. This algorithm has been applied in supervised, semi-supervised and unsupervised forms. It provides solutions for forward and inverse modeling within a unified optimization framework. These modeling techniques, whether for forward or inverse problems, are strongly based on data-driven principles and data-driven discovery. PINN showcases its adaptability by accommodating both continuous and discrete forms of PDEs for both forward and inverse modeling endeavors. Continuous time-dependent model approximation relies on spatio-temporal function estimation. On the other hand, when dealing with discrete time modeling, it tackles exact implicit Runge-Kutta time-stepping techniques, supporting an unrestricted number of time increments. This novel algorithm has extended [20], [21], [39] and [49] and authors also provided a library to solve PDE with PINN [28]. [11] and [32] modified this algorithm with domain decomposition approach. [9] and [8] gives the theoretical error bound of [20]. More importantly, there still needs to be more understanding of why these models occasionally fail to train. [43] explore these issues by examining them through the framework of the neural tangent kernel.

A technique involves utilizing deep neural networks (DNNs) that are founded on explicit or partially explicit representation formulas applicable to parabolic and elliptic partial differential equations (PDEs). Researchers leverage this compositional structure to enhance the approximation capabilities of deep neural networks (DNNs). Researchers such as [18], [13], and [5], among others, have introduced and examined this technique for a range of parametric elliptic and parabolic PDEs. In [22], authors discussed a similar approach for approximating linear transport equations with DNNs. The application of deep learning using DNNs has revolutionized numerous domains, including image and text categorization, machine vision, computational linguistics, voice recognition, self-governing systems, robotics, artificial intelligence in gaming, medical analysis, pharmaceutical research, climate simulation, financial prediction, and protein structure determination. These advancements highlight the versatility

and effectiveness of DNNs in tackling complex problems across diverse domains. A recent study by Mishra and Molinaro examines the generalization error of addressing forward problems [31] and inverse problems [30] across various linear and nonlinear partial differential equations (PDEs). The authors have also estimated generalized error bounds for the problems. The authors also worked for simulating radiative transfer [29] and nonlinear dispersive PDEs [2]. [29] and [2] also derive generalized error bounds for forward problems. The study investigates the stability characteristics of the underlying PDE, utilizing these features to assess generalization errors in connection with training errors and the training dataset’s magnitude. Furthermore, [10] introduces an innovative modification of PINNs called weak PINNs (wPINNs).

Mishra et al. [29] proposed a PINN-based algorithm for simulating radiation transport. The work addresses both forward and inverse problems and establishes generalized error bounds for forward problems. This framework is particularly relevant for leveraging machine learning approaches in solving complex physical systems governed by differential equations. Huhn et al. [19] simulated one-dimensional radiation transport in heterogeneous media using a PINN algorithm with Fourier features. Riganti et al. [37] addressed forward, inverse, and coupled radiation transport problems using an auxiliary PINN. Xie et al. [45] simulated neutron transport equation with boundary-dependent PINN. The primary goal of our article is to simulate the underlying PDEs using both forward and inverse methods and to establish the generalization error bounds. We have used unsupervised PINN algorithms. In this work, new models for the medium have been developed and simulated. Additionally, predefined challenging models have also been simulated in this study. The results obtained demonstrate improved performance compared to numerical schemes such as the finite element methods (e.g., GFEM, LSFEM, and discontinuous finite element method), meshfree methods, and MRT lattice Boltzmann method. We employed novel PINN algorithms to address and overcome the above mentioned difficulties. We successfully mitigated the challenges associated with traditional methods, achieving results without spurious wiggles. Minimal errors were observed, slightly increasing with the rise of optical thickness.

The work is divided as following :The first section describes an introduction and examines pertinent literature. The second section outlines the mathematical model and methodological approach, denoted as a problem statement and PINN approximation. This section is divided into eight components: the model, the underlying model and domain, quadrature rules, training points, neural networks, residuals, loss functions, optimization, estimation of generalization error, and the steady-state behavior of the model. The third part is dedicated to confirming the precision of the suggested method, followed by an investigation into radiation behavior within graded-index media, accompanied by numerical simulations. In the fourth part, we add the conclusion. In the end, we also added an appendix to estimate generalization errors. The impact of different optical parameters on radiometric quantities is then analyzed and confirmed.

## 2 Problem statement and PINN approximation

Precise prediction of radiative transfer in these circumstances relies on resolving the Radiative Transfer Equation (RTE), an intricate integro differential equation encompassing seven variables: three spatial coordinates, polar and azimuthal angles, time, and spectral dimensions. The complexity increases in graded index media, where the curved radiation path, described by the Fermat principle, introduces an additional layer of intricacy, rendering analytical solutions unattainable except in specific limiting cases. Therefore, developing accurate, simple, and efficient tools to solve the RTE in these scenarios becomes imperative for advancing understanding and practical applications. Snell’s Law and the Fermat principle [25] are closely related concepts that describe different aspects of light propagation but are fundamentally connected. Snell’s Law [1] quantitatively describes how light bends or refracts when transitioning between different optical mediums with varying refractive indices. It defines a mathematical connection between the angles of incidence and refraction. In the context of Snell’s Law, the light path between two points is the one that reduces the time needed for light to travel from the source to the observer, considering the changes in the refractive index along the way. Therefore, while Snell’s Law quantifies the angle of refraction at the boundary between two mediums, the Fermat principle explains why light follows this particular path by minimizing the time it takes to travel between two points. In media with graded indices, where the refractive index changes spatially, the Fermat principle affects the path of light rays, resulting in curved trajectories explained by Snell’s Law.

Figure 1 illustrates the fundamental concept of Snell’s law [41]. In graded-index media, light rays follow a curved path dictated by the Fermat principle. This leads to a more complex radiative transfer solution compared to uniform-index media. Typically, in such instances, the refractive index varies from the center of the material to its surface.

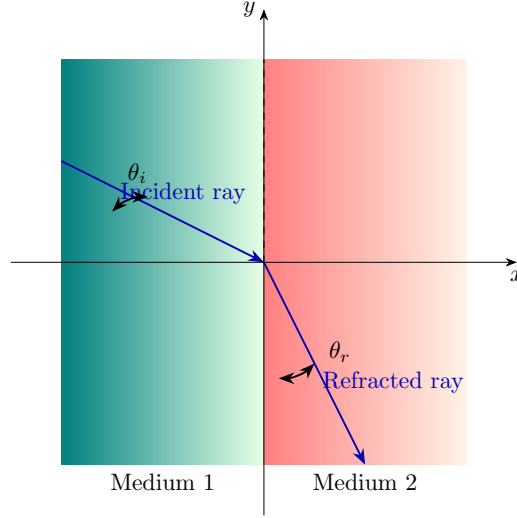


Figure 1: An illustration of a Snell's law.

## 2.1 The model

### Radiation transport equation in graded index media

The radiation transport equation for graded-index media, which describes the distribution of radiative intensity  $I(s, \mathbf{\Omega}, t)$  at position  $s$  and time  $t$  in the direction  $\mathbf{\Omega}(\theta, \varphi)$ , is given as [48].

$$\frac{n}{c_0} \frac{\partial}{\partial t} I(s, \mathbf{\Omega}, t) + (k_e + \mathbf{\Omega} \cdot \nabla) I(s, \mathbf{\Omega}, t) + \frac{1}{n \sin \theta} \cdot I_\theta + \frac{1}{n \sin \theta} \cdot I_\varphi = \mathcal{S}(s, \mathbf{\Omega}, t), \quad (2.1)$$

Where  $I_\theta = \frac{\partial}{\partial \theta} \{I(s, \mathbf{\Omega}, t)(\mathbf{\Omega} \cos \theta - k) \cdot \nabla n\}$  and  $I_\varphi = \frac{\partial}{\partial \varphi} \{(s_1 \cdot \nabla n) I(s, \mathbf{\Omega}, t)\}$ . Here,  $n$ ,  $s$ , and  $k_e$  are the refractive index, position vector, and extinction coefficient.  $\mathbf{\Omega} = i \sin \theta \cos \varphi + j \sin \theta \sin \varphi + k \cos \theta$  is the direction vector, and  $s_1 = k \times \frac{\mathbf{\Omega}}{|k \times \mathbf{\Omega}|} = -i \sin \varphi + j \cos \varphi$ , where  $i$ ,  $j$ , and  $k$  signify the unit vectors in the coordinate system. The sum of coefficients  $k_a$  (absorption) and  $k_s$  (scattering) represent extinctions coefficients. The sum of  $k_a$  and  $k_s$  equals the extinction coefficients  $k_e$ . The single scattering albedo can be expressed as  $\omega = \frac{k_s}{k_e}$ . The source term  $\mathcal{S}(s, \mathbf{\Omega}, t)$  is provided as [48], [44]

$$\mathcal{S}(s, \mathbf{\Omega}, t) = n^2 k_a I_b(T_g) + \frac{k_s}{4\pi} \int_{4\pi} \Phi(\mathbf{\Omega}' \rightarrow \mathbf{\Omega}) I(s, \mathbf{\Omega}', t) d\mathbf{\Omega}',$$

where  $T_g$  denote medium temperature. Scattering phase function  $\Phi(\mathbf{\Omega}' \rightarrow \mathbf{\Omega})$  describes the energy redistribution from the incoming direction  $\mathbf{\Omega}'(\theta', \varphi')$  to the outgoing direction  $\mathbf{\Omega}(\theta, \varphi)$ .

Boundary conditions of the model are  $\mathbf{\Omega} \cdot \hat{\mathbf{n}}_\omega < 0$  and  $\mathbf{\Omega}_{r_s} \cdot \hat{\mathbf{n}}_\omega < 0$ . In this context,  $\hat{\mathbf{n}}_\omega$  is the normal vector that points outward from the surface. The direction  $\mathbf{\Omega}_{r_s} = \mathbf{\Omega} - 2(\mathbf{\Omega} \cdot \hat{\mathbf{n}}_\omega) \hat{\mathbf{n}}_\omega$  represents the incident direction for specular reflection. The boundary intensity for  $\mathbf{\Omega}_{r_s} \cdot \hat{\mathbf{n}}_\omega < 0$  is

$$I(s_\omega, \mathbf{\Omega}, t) = Q_{ext} + \rho_\omega^{spec} I(s_\omega, \mathbf{\Omega}_s, t) + n_\omega^2 \varepsilon_\omega I_{b_\omega} + \frac{\rho_\omega^d}{\pi} \int_{\mathbf{\Omega}' \cdot \hat{\mathbf{n}}_\omega > 0} |\mathbf{\Omega}' \cdot \hat{\mathbf{n}}_\omega| I(s_\omega, \mathbf{\Omega}', t) d\mathbf{\Omega}',$$

Where  $I_{b_\omega}$  represents the black-body intensity at the boundary, while  $\rho_\omega^{spec}$  and  $\rho_\omega^d$  denote the specular and diffuse reflectivities of the boundary, respectively, with emissivity  $\varepsilon_\omega$ . The external driving force  $Q_{ext}$  is incoming from the external side of the boundary at a direction  $\mathbf{\Omega}_0$  as described by Snell's law. From the RTE, the radiative flux vector  $q(s, t)$  and the incident radiation  $G(s, t)$  at any point  $M(x, y)$  can be computed as follows:

$$q(s, t) = \int_{4\pi} \mathbf{\Omega} I(s, \mathbf{\Omega}, t) d\mathbf{\Omega}, \quad G(s, t) = \int_{4\pi} I(s, \mathbf{\Omega}, t) d\mathbf{\Omega}.$$

Laser irradiation's collimated intensity  $I_c$  experiences attenuation as it travels through the medium. This can be solved analytically within the medium, with the boundary condition  $I_c(s_\omega, \mathbf{\Omega}, t) = Q_{ext}$ . The reduction in

collimated intensity  $I_c$  in the medium results in the generation of diffuse intensity  $I_d(s, \mathbf{\Omega}, t)$ . Consequently, the total intensity  $I(s, \mathbf{\Omega}, t)$  comprises both collimated and diffuse components, expressed as:

$$I(s, \mathbf{\Omega}, t) = I_c(s, \mathbf{\Omega}, t) + I_d(s, \mathbf{\Omega}, t).$$

This equation represents the transport equation for graded-index media and is a fundamental framework for modeling radiation transport in such materials.

## 2.2 The underlying model and domain

We can modified  $I(t, s, \mathbf{\Omega})$  as  $I(t, s, \mathbf{\Omega}, \xi)$ , where group energy  $\xi \in \Pi \subset \mathbb{R}$ ,  $\mathbf{\Omega} \in S \subset$  unit sphere(d dimensional),  $\Omega \in S \times \Pi$ ,  $t \in [0, T]$ , spatial variable  $s \in D \subset \mathbb{R}^d$ ,  $D_T = [0, T] \times D$ ,  $I : [0, T] \times D \times S \times \Pi \rightarrow \mathbb{R}$ ,  $k_e = k(s, \xi) : D \times \Pi \rightarrow \mathbb{R}_+$ ,  $k_a = k(s, \xi) : D \times \Pi \rightarrow \mathbb{R}_+$ ,  $k_s = k(s, \xi) : D \times \Pi \rightarrow \mathbb{R}_+$ ,  $\Phi : S \times S \times \Pi \times \Pi \rightarrow \mathbb{R}$ , Integral of  $\Phi(\theta, \theta', \varphi, \varphi')$  over  $S \times \Pi$  is equal to 1.

Here, the underlying model will be defined for two approaches: the data-driven approach so called forward problem, and the data driven discovery approach, also referred to as data assimilation or the inverse problems.

### 2.2.1 The underlying model for forward problem

Here, we will define the radiation transport equation with supplemented initial conditions(I.C.) and boundary conditions(B.C.). The defined partial integrodifferential supplied the I.C. and B.C., which are the following:

**I.C.**

$$I(0, s, \mathbf{\Omega}, \xi) = I_0(s, \mathbf{\Omega}, \xi) \quad \text{where } (s, \mathbf{\Omega}, \xi) \in D \times S \times \Pi, \quad (2.2)$$

And  $I_0 : D \times S \times \Pi \rightarrow \mathbb{R}$ ,

**B.C.**

$$\beta = \{(t, s, \mathbf{\Omega}, \xi) \in [0, T] \times \partial D \times S \times \Pi : \mathbf{\Omega} \cdot \hat{\mathbf{n}}_\omega < 0\}. \quad (2.3)$$

We can wrote  $I(t, s, \mathbf{\Omega}, \xi) = I_b(t, s, \mathbf{\Omega}, \xi)$  for some B.C, we can wrote  $I_b : \beta \rightarrow \mathbb{R}$ .

### 2.2.2 The underlying model for inverse problem

The underlying equation with solution  $I$  is considered within the subdomain  $D'_T \times S \times \Pi$ . This assumption holds that the operator  $\mathcal{L}$  applied to  $I$  in this region equals a given data  $g$ . Mathematically, it can be denoted as:

$$\mathcal{L}(I) = g, \quad \forall (s, \mathbf{\Omega}, \xi) \in D'_T \times S \times \Pi,$$

Where  $D' \subset D$ ,  $D'_T = [0, T] \times D'$  and  $g$  is a source term.

## 2.3 Quadrature rules

Following the approaches outlined in [29–31], let  $\mathbf{D}$  represent a domain and  $\varrho$  be an integrable function defined as  $\varrho : \mathbf{D} \rightarrow \mathbb{R}$ . Consider the space-time domain  $D_T = [0, T] \times D \subset \mathbb{R}^{\bar{d}}$ , where  $\bar{d} = 2d + 1 \geq 1$ . We define a mapping  $\varrho : \mathbf{D} \rightarrow \mathbb{R}$ , where

$$\varrho = \int_{\mathbf{D}} \varrho(y) dy, \quad (2.4)$$

with  $dy$  representing the  $\bar{d}$ -dimensional Lebesgue measure. To approximate this integral, we utilize quadrature points  $y_i \in \mathbf{D}$  for  $1 \leq i \leq N$ , along with their corresponding weights  $w_i$ . The quadrature approximation of  $\varrho$  is expressed as:

$$\varrho_N = \sum_{i=1}^N w_i \varrho(y_i), \quad (2.5)$$

Here,  $y_i$  represents the quadrature points. For cases where  $\bar{d} \leq 4$ , standard composite Gauss quadrature rules can be applied using an underlying grid. The selection of quadrature points and weights depends on the order of the quadrature rule, as outlined in [40]. However, Gauss quadrature becomes inefficient for higher-dimensional domains. In cases of moderate dimensionality ( $4 \leq \bar{d} \leq 20$ ), low-discrepancy sequences, such as Sobol and Halton sequences, are effective for selecting quadrature points, assuming that the function  $\varrho$  has a bounded Hardy-Krause variation [6]. In cases of high dimensionality (when  $d \gg 20$ ), Monte Carlo quadrature is the favored approach,

exacting randomly chosen quadrature points that are independent and identically distributed(i.i.d.) [6]. Let  $\mathbf{S}$  represent a training dataset, and define the space-time domain as  $D_T = [0, T] \times D$ . The selection of training set  $\mathbf{S} \subseteq [0, T] \times D$  will be depend on appropriate quadrature points. For the PINN algorithms, we choose random points  $y_i^a = (\Omega_i^S, \xi_i^S)$  for  $1 \leq i \leq N_S$ , where  $w_i^S$  represents the corresponding quadrature weights, and  $a \geq 1$ . The Quasi-Monte Carlo (QMC) quadrature method remains unaffected by the curse of dimensionality. In situations where the geometry of the domain is particularly intricate, random points can be chosen as training samples, which i.i.d. according to the underlying uniform distribution.

## 2.4 Training points

Physics informed neural networks require four types of training points as described in [29, 30]: interior points  $\zeta_{\text{int}}$ , temporal boundary points  $\zeta_{\text{tb}}$ , spatial boundary points  $\zeta_{\text{sb}}$ , and data points  $\zeta_d$ . Figs.2 and 3 illustrate the training points used in forward and inverse problems, respectively.

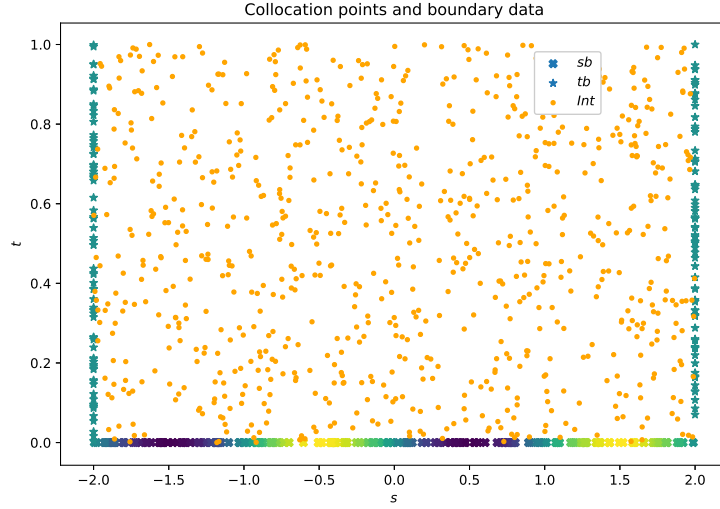


Figure 2: Training points (forward problem): A depiction of the training set  $\mathbf{S}$  with randomly selected training points. Yellow dots represent interior points, while green and blue dots indicate the temporal and spatial boundary points.

### 2.4.1 Interior training points

The interior training points are denoted by  $\zeta_{\text{int}} = \{z_j^{\text{int}}\}$  for  $1 \leq j \leq N_{\text{int}}$ , where  $z_j^{\text{int}} = (t_j^{\text{int}}, s_j^{\text{int}}, \Omega_j^{\text{int}}, \xi_j^{\text{int}})$ . Here,  $t_j^{\text{int}} \in [0, T]$ ,  $s_j^{\text{int}} \in D$ ,  $\Omega_j^{\text{int}} \in S$ , and  $\xi_j^{\text{int}} \in \Pi$  for all  $j$ . These points correspond to quadrature points with weights  $w_j^{\text{int}}$  based on a suitable quadrature rule. In domains  $D$  that are logically rectangular, one can either use Sobol points or randomly select points to create the training set.

### 2.4.2 Temporal boundary training points

The temporal boundary points are represented as  $\zeta_{\text{tb}} = \{z_j^{\text{tb}}\}$ , for  $1 \leq j \leq N_{\text{tb}}$ , with  $z_j^{\text{tb}} = (s_j^{\text{tb}}, \Omega_j^{\text{tb}}, \xi_j^{\text{tb}})$ . Here,  $s_j^{\text{tb}} \in D$ ,  $\Omega_j^{\text{tb}} \in S$ , and  $\xi_j^{\text{tb}} \in \Pi \forall j$ . The designated points function as quadrature points within an appropriate quadrature rule, accompanied by weights denoted as  $w_j^{\text{tb}}$ . For logically rectangular domains  $D$ , Sobol points can be chosen, or alternatively, random points can be employed to construct the training dataset, similar to previous method.

### 2.4.3 Spatial boundary training points

The spatial boundary points are denoted as  $\zeta_{\text{sb}} = \{z_j^{\text{sb}}\}$ , for  $1 \leq j \leq N_{\text{sb}}$ , where  $z_j^{\text{sb}} = (t_j^{\text{sb}}, s_j^{\text{sb}}, \Omega_j^{\text{sb}}, \xi_j^{\text{sb}})$ . In this case,  $t_j^{\text{sb}} \in [0, T]$ ,  $s_j^{\text{sb}} \in \partial D$ ,  $\Omega_j^{\text{sb}} \in S$ , and  $\xi_j^{\text{sb}} \in \Pi$ . For logically rectangular domains  $D$ , Sobol points can be chosen, or alternatively, random points can be employed to construct the training dataset, similar to previous method.

### 2.4.4 Data training points

The data training set is defined as  $\zeta_{\mathbf{d}} = \{z_j^{\mathbf{d}}\}$  for  $1 \leq j \leq N_{\mathbf{d}}$ , where  $z_j^{\mathbf{d}} \in D' \subset D$ .

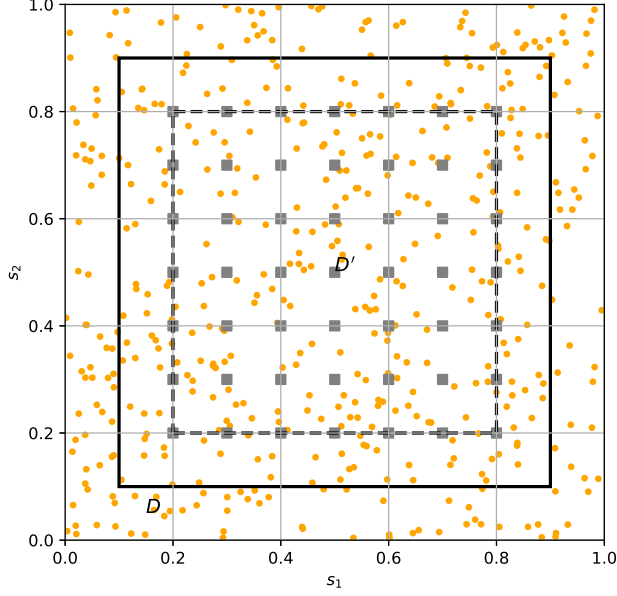


Figure 3: Training points (inverse problem): A representation of the training set  $\mathcal{S}$  with randomly selected training points. Yellow dots indicate interior points, and grey dots represent Sobol points.

## 2.5 Neural networks

The PINN functions as a feed-forward neural network, as illustrated in Fig. 4. A neural network without an activation function behaves as a simple multiple regression model. However, the activation function adds non-linearity, allowing the network to learn and execute more complex tasks. The sigmoid, hyperbolic tangent (tanh), and ReLU functions are some examples of activation functions [17].

The input to the network is  $z = (t, s, \Omega, \xi) \in \mathbf{D} = [0, T] \times D \times S \times \Pi$ . The neural network can be expressed as an affine map:

$$I_{\Theta}(z) = C_K \circ \sigma \circ C_{K-1} \circ \dots \circ \sigma \circ C_1(z). \quad (2.6)$$

Where  $\circ$  and  $\sigma$  are composition of functions and activation function respectively. For any layer  $k$  such that  $1 \leq k \leq K$ , the transformation at the  $k$ -th layer is defined as follows:

$$C_k y_k = W_k y_k + b_k \quad \text{where} \quad W_k \in \mathbb{R}^{d_{k+1} \times d_k}, \quad y_k \in \mathbb{R}^{d_k}, \quad \text{and} \quad b_k \in \mathbb{R}^{d_{k+1}}. \quad (2.7)$$

To ensure consistency, we establish  $d_1 = \bar{d} = 2d + 1$ , where  $d$  represents the spatial dimension, and we define  $d_K = 1$  for the output layer. In the context of machine learning, this neural network consists of an input layer, an output layer, and  $K - 1$  hidden layers, with the condition that  $1 < K < \mathbb{N}$ . Each hidden layer  $k$ , which consists of  $d_k$  neurons, takes an input vector  $y_k \in \mathbb{R}^{d_k}$ . Initially, this input vector is transformed using the linear mapping  $C_k$ , after which it is processed by a non-linear activation function represented as  $\sigma$ . The overall count of neurons in the network can be expressed as  $2d + 2 + \sum_{k=2}^{K-1} d_k$ . We define the parameter set for the network, which includes weights and biases, as  $\Theta = \{W_k, b_k\}$ . Furthermore, we denote the set of weights as  $\Theta_w = \{W_k\}$  for all  $1 \leq k \leq K$  [29, 30]. The parameters  $\Theta$  lie in the space  $\Theta' \subset \mathbb{R}^P$ , and  $P$  denote total number of parameters:

$$P = \sum_{k=1}^{K-1} (d_k + 1) d_{k+1}. \quad (2.8)$$

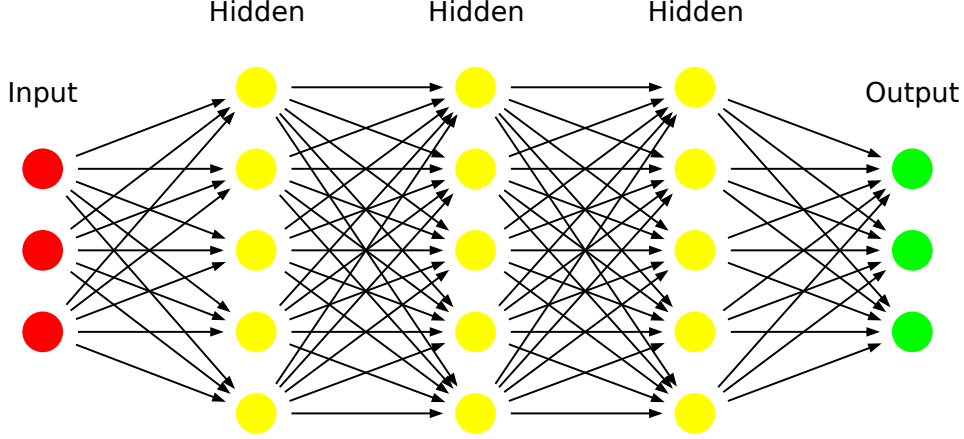


Figure 4: In this diagram, input layer neurons are depicted in red, hidden layer neurons in yellow, and output layer neurons in green.

## 2.6 Residuals

This section outlines the residuals associated with the divided training sets, including interior, temporal, data (for inverse), and spatial training points. The focus is on minimizing these residuals. Optimization techniques will involve stochastic gradient descent methods, such as ADAM for first-order optimization, and higher-order approaches like variations of the BFGS algorithm. The PINN  $I_\Theta$  depends on tuning parameters  $\Theta \in \Theta'$ , which represent the weights and biases within the network. In a typical deep learning setup, the network is trained by optimizing these parameters  $\Theta$  to ensure that the neural network approximation  $I_\Theta$  accurately aligns with the exact solution  $I$ . The interior residual can be written as:

$$R_{\text{int},\Theta} = R_{\text{int},\Theta}(t, s, \mathbf{\Omega}, \xi), \quad \forall (t, s, \mathbf{\Omega}, \xi) \in [0, T] \times D \times S \times \Pi, \quad (2.9)$$

We can express the interior residual  $R_{\text{int},\Theta}$  as:

$$\begin{aligned} R_{\text{int},\Theta} = & \frac{n}{c_0} \frac{\partial}{\partial t} I_\Theta + (k_e + \mathbf{\Omega} \cdot \nabla) I_\Theta + \frac{1}{n \sin \theta} \frac{\partial}{\partial \theta} \{ I_\Theta (\mathbf{\Omega} \cos \theta - k) \cdot \nabla n \} \\ & + \frac{1}{n \sin \theta} \frac{\partial}{\partial \varphi} \{ (s_1 \cdot \nabla n) I_\Theta \} - n^2 k_a I_{b\Theta}(T_g) - \frac{k_s}{4\pi} \sum_{i=1}^{N_S} w_i^S \Phi(\mathbf{\Omega}, \mathbf{\Omega}_i^S, \xi, \xi_i^S) I_\Theta, \end{aligned} \quad (2.10)$$

In this equation,  $(\mathbf{\Omega}_i^S, \xi_i^S)$  represent the Gauss-Legendre quadrature points, while  $w_i$  signify the corresponding quadrature weights of order  $S$ . The residuals for the initial, boundary, and data points are defined as follows:

$$\begin{aligned} R_{\text{tb}} = R_{\text{tb},\Theta} = I_\Theta - I_0, \quad \forall (s, \mathbf{\Omega}, \xi) \in D \times S \times \Pi, \\ R_{\text{sb}} = R_{\text{sb},\Theta} = I_\Theta - I_b, \quad \forall (t, s, \mathbf{\Omega}, \xi) \in \beta. \end{aligned} \quad (2.11)$$

And

$$R_{\mathbf{d}} = \mathcal{L}(I_\Theta) - g, \quad \forall (s, \mathbf{\Omega}, \xi) \in D'_T \times S \times \Pi. \quad (2.12)$$

Our aim is to find the optimal set of tuning parameters  $\Theta \in \Theta'$  that minimizes the residual specified in the forward problem equation,

$$\Theta^* \in \Theta' : \Theta^* = \arg \min_{\Theta \in \Theta'} \left( \|R_{\text{int},\Theta}\|_{L^2([0,T] \times D \times S \times \Pi)}^2 + \|R_{\text{sb},\Theta}\|_{L^2(\beta)}^2 + \|R_{\text{tb},\Theta}\|_{L^2(D \times S \times \Pi)}^2 \right). \quad (2.13)$$

For the inverse problem, we add the term corresponding to the data residual  $R_{\mathbf{d}}$  to Eq.(2.13). This results in the following minimization problem:

$$\Theta^* \in \Theta' : \Theta^* = \arg \min_{\Theta \in \Theta'} \left( \|R_{\text{int},\Theta}\|_{L^2(D_T \times S \times \Pi)}^2 + \|R_{\text{sb},\Theta}\|_{L^2(\beta)}^2 + \|R_{\mathbf{d},\Theta}\|_{L^2(D'_T \times S \times \Pi)}^2 \right). \quad (2.14)$$

The integrals in Eqs.(2.13) and (2.14) cannot be calculated exactly due to the use of the  $L^2$  norm, necessitating approximation through an appropriate quadrature method.



## 2.7 Loss functions and optimization

We approximate the above integral with the following loss functions for forward and inverse problems, respectively

$$\mathcal{F}_1(\Theta) = \sum_{j=1}^{N_{sb}} w_j^{sb} |R_{sb,\Theta}(z_j^{sb})|^2 + \sum_{j=1}^{N_{tb}} w_j^{tb} |R_{tb,\Theta}(z_j^{tb})|^2 + \lambda \sum_{j=1}^{N_{int}} w_j^{int} |R_{int,\Theta}(z_j^{int})|^2, \quad (2.15)$$

$$\mathcal{F}_2(\Theta) = \sum_{j=1}^{N_d} w_j^d |R_{d,\Theta}(z_j^d)|^2 + \sum_{j=1}^{N_{sb}} w_j^{sb} |R_{sb,\Theta}(z_j^{sb})|^2 + \lambda \sum_{j=1}^{N_{int}} w_j^{int} |R_{int,\Theta}(z_j^{int})|^2, \quad (2.16)$$

Regularize the minimization problems for the loss function, i.e

$$\Theta^* = \arg \min_{\Theta \in \Theta'} (\mathcal{F}_i(\Theta) + \lambda_{reg} \mathcal{F}_{reg}(\Theta)), \quad (2.17)$$

Where  $i = 1, 2$ . In machine learning, it is common to incorporate a regularization term to mitigate overfitting. A widely used form of the regularization function is  $\mathcal{F}_{reg}(\Theta) = \|\Theta\|_q^q$ , where  $q$  is typically 1 (for  $L^1$  regularization) or 2 (for  $L^2$  regularization). The parameter  $\lambda_{reg}$  controls the balance between the regularization term and the actual loss function  $\mathcal{F}$ , with  $0 \leq \lambda_{reg} \ll 1$ . Stochastic gradient descent methods, including ADAM, will be applied due to their popularity in first-order optimization. Additionally, advanced optimization techniques, including various forms of the BFGS algorithm, may be employed. Our aim is to identify the optimal solution  $I^* = I_{\Theta^*}$  using the training sets. We begin with an initial value  $\bar{\Theta} \in \Theta'$  and calculate the network output  $I_{\bar{\Theta}}$ , PDE residual, boundary residual, loss function, and its gradients. Ultimately, the optimal solution is  $I^* = I_{\Theta^*}$ , which is determined by the PINN.

We approximate local minimum in (2.17) as  $\Theta^*$ . The resulting DNNs  $I^* = I_{\Theta^*}$  will solution  $I$  of (2). The Table1 contains a hyperparameter of numerical experiments. We provide a summary of the PINN algorithms for approximating RTE in a graded index medium. The algorithms are described in [29], [30], [2], and [31]. Below, Algorithm 2.1 is presented for forward problems, while Algorithm 2.2 addresses inverse problems:

Table 1: The configurations of hyperparameters and the frequency of retraining utilized in ensemble training for physics-informed neural networks (PINN).

Examples	$K - 1$	$\bar{d}$	$\lambda$	$\lambda_{reg}$	$n_{\Theta}$
Example 1a,b,c	4, 8	20, 24	0.1, 1, 10	0	4
Example 2a,b,c,d	4, 8	24, 28	0.1, 1, 10	0	10,10,4,4
Example 3a,b,c	4, 8	24, 28	0.1, 1, 10	0	4
Example 4a,b,c	4, 8	20, 24	0.1, 1, 10	0	4
Example 5a, b	4, 8	20, 24	0.1, 1, 10	0	4
Example 6a, b	4, 8	20, 24	0.1, 1, 10	0	4,5

### Algorithm 2.1. Algorithm for developing a PINN to estimate radiative intensity in forward problems.

**Inputs:** Underlying domain, data, and coefficients for the RTE with graded index Eq.(2); quadrature points and weights for the underlying quadrature rules; non-convex gradient-based optimization algorithms.

**Aim:** To approximate the solution of the model, using a PINN  $I^* = I_{\Theta^*}$ .

**Step 1:** Select the training sets as outlined in section 2.4.

**Step 2:** Initialize with a weight vector  $\bar{\Theta} \in \Theta'$  and calculate: neural network  $I_{\bar{\Theta}}$  Eq.(2.6), PDE residual Eq.(2.10), boundary residuals Eq.(2.11), loss function Eq.(2.15), Eq.(2.17), and gradients for optimization algorithm initiation.

**Step 3:** Execute the optimization algorithm until reaching an approximate local minimum  $\Theta^*$  of Eq.(2.17). The resulting function  $I^* = I_{\Theta^*}$  is the desired PINN for approximating the radiative transfer equation solution  $I$ .

## 2.8 Estimation on generalization error

Let the spatial domain be  $D = [0, 1]^d$ , where  $d$  denote the spatial dimension. This section focuses on obtaining an accurate estimation of the generalization error or so called total error for the trained neural network,  $I^* = I_{\Theta^*}$ . This result arises from the application of the PINNs algorithms 2.1 and 2.2. The error can be expressed as follows:

$$E_G = E_G(\theta^*) = \left( \int_{\mathbf{D}} |I(t, s, \Omega, \xi) - I^*(t, s, \Omega, \xi)|^2 dX \right)^{\frac{1}{2}} \quad (2.18)$$

Where  $dX = dt ds d\Omega d\xi$  denotes the volume measure on  $\mathbf{D}$ . This approach outlined in [29], [2], [30], and [31]. This section provides an estimation of the generalization error, as defined in equation (2.18), based on the training error.

$$\begin{aligned} E_T^{N_{sb}} &= \left( \sum_{j=1}^{N_{sb}} w_j^{sb} |R_{sb, \Theta^*}(z_j^{sb})|^2 \right)^{\frac{1}{2}}, E_T^{N_{tb}} = \left( \sum_{j=1}^{N_{tb}} w_j^{tb} |R_{tb, \Theta^*}(z_j^{tb})|^2 \right)^{\frac{1}{2}}, \\ E_T^{N_{int}} &= \left( \sum_{j=1}^{N_{int}} w_j^{int} |R_{int, \Theta^*}(z_j^{int})|^2 \right)^{\frac{1}{2}}, E_T^{N_d} = \left( \sum_{j=1}^{N_d} w_j^d |R_{d, \Theta^*}(z_j^d)|^2 \right)^{\frac{1}{2}}. \end{aligned} \quad (2.19)$$

The generalized error is similar to the form presented in [29] and is expressed as:

$$\begin{aligned} (E_G)^2 &\leq V \left( (E_T^{tb})^2 + v (E_T^{sb})^2 + c (E_T^{int})^2 \right) \\ &+ VV_2 \left( \frac{(\log(N_{tb}))^{2d}}{N_{tb}} + c \frac{(\log(N_{sb}))^{2d}}{N_{sb}} + c \frac{(\log(N_{int}))^{2d+1}}{N_{int}} + c N_S^{-2a} \right). \end{aligned} \quad (2.20)$$

Where  $V_2, v$ , and  $V$  are constants as defined in Appendix Appendix D.1. Consider  $\Phi$  is symmetric such that

$$\Phi(\Omega, \Omega', \xi, \xi') = \Phi(\xi, \xi', \Omega, \Omega'),$$

And let

$$\Sigma_g(\Omega, \xi) = \int_{4\pi} \Phi(\Omega, \Omega', \xi, \xi') d\Omega'$$

Where  $S \times \Pi \in \Omega'$  and  $\Sigma_g$  is essentially bounded i.e  $\Sigma_g \in L^\infty(S \times \Pi)$ .

**Algorithm 2.2. Algorithm for developing a PINN to estimate radiative intensity in inverse problems.**

**Inputs:** Underlying domain, data, and coefficients for the RTE with graded index Eq.(2); appropriate quadrature points and weights for the underlying quadrature rules; and non-convex gradient-based optimization algorithms.

**Aim:** To approximate the solution  $I$  of Eq.(2) for inverse problems, using a PINN  $I^* = I_{\Theta^*}$ .

**Step 1:** Select the training sets outline in Section 2.4.

**Step 2:** Initialize with a weight vector  $\bar{\Theta} \in \Theta'$  and calculate: neural network  $I_{\bar{\Theta}}$  Eq.(2.6), PDE residual Eq.(2.10), data residuals Eq.(2.12), loss function Eq. (2.16), Eq.(2.17) and gradients for optimization algorithm initiation.

**Step 3:** Execute the optimization algorithm until reaching an approximate local minimum  $\Theta^*$  of Eq.(2.17). The resulting function  $I^* = I_{\Theta^*}$  is the desired PINN for approximating the radiative transfer equation solution  $I$ .

## 2.9 Steady case

If  $c_0 \rightarrow \infty$ , Eq.(2) becomes

$$(k_e + \Omega \cdot \nabla)I + \frac{1}{n \sin \theta} \cdot I_\theta + \frac{1}{n \sin \theta} \cdot I_\varphi = \mathcal{S}, \quad (2.21)$$

### B.C.

$$\beta_o = \{(s, \Omega, \xi) \in \partial D \times S \times \Pi : \Omega \cdot \hat{n}_\omega < 0\}, \quad (2.22)$$

We can write  $I(s, \Omega, \xi) = I_b(s, \Omega, \xi)$  for some B.C., we can write  $I_b : \beta_o \rightarrow \mathbb{R}$ . Let  $D = [0, 1]^d$ , where  $d$  denotes spatial dimension. This section aims to derive a precise generalization error estimate for the trained neural network  $I^* = I_{\Theta^*}$ . This network is the result of the PINNs algorithms described in algorithms 2.1 and 2.2.

$$E_{G_{steady}} = E_G(\theta^*) = \left( \int_{D \times S \times \Pi} |I(s, \Omega, \xi) - I^*(s, \Omega, \xi)|^2 dX \right)^{\frac{1}{2}}, \quad (2.23)$$

Where  $dX = dsd\Omega d\xi$ ,

$$\begin{aligned} E_T^{N_{sb}} &= \left( \sum_{j=1}^{N_{sb}} w_j^{sb} \left| R_{sb, \Theta^*}(z_j^{sb}) \right|^2 \right)^{\frac{1}{2}}, E_T^{N_{int}} = \left( \sum_{j=1}^{N_{int}} w_j^{int} \left| R_{int, \Theta^*}(z_j^{int}) \right|^2 \right)^{\frac{1}{2}}, \\ E_T^{N_d} &= \left( \sum_{j=1}^{N_d} w_j^d \left| R_{d, \Theta^*}(z_j^d) \right|^2 \right)^{\frac{1}{2}}. \end{aligned} \quad (2.24)$$

The generalized error is similar to the form presented in [29] and is expressed as:

$$\begin{aligned} (E_{G_{steadyf}})^2 &\leq V \left( \nu (E_T^{sb})^2 + \nu (E_T^{int})^2 \right) \\ &+ V \left( \frac{(\log(N_{sb}))^{2d}}{N_{sb}} + \nu \frac{(\log(N_{int}))^{2d}}{N_{int}} + \nu N_S^{-2a} \right), \end{aligned} \quad (2.25)$$

Where  $\nu$  and  $V$  are constants as defined in Appendix Appendix D.2.

The generalization error bound express the approximation error for the underlying problems using a trained PINN will remain small if certain conditions are satisfied:

**Remark 2.3.** The PINN should be effectively trained, as evidenced by a sufficiently small training error. Although the training error cannot be controlled *a priori*, it can be computed *a posteriori*. A sufficiently large number of training (collocation) points is necessary to ensure accurate learning. The quadrature error, which depends on the number of collocation points  $N$  and the quadrature constants, can be reduced by selecting a large enough  $N$ . This finding underscores that the generalization error estimate sets an upper bound on the total error, encompassing both training errors (from equations 2.19 and 2.24) and the number of training data points  $N_{int}, N_{sb}, N_{tb}$ , as well as the quadrature points  $N_S$  utilized to approximate the scattering integral (from equation 2). Although no *a priori* estimate is available for the training errors, they can be computed after complete training. Therefore, the theorems suggest that the model will generalize effectively if the involved constants remain finite and the PINN is trained adequately. This aligns with general machine learning theory, where a well-trained and regularized PINN  $I^*$  ensures stability and bounded generalization error. Here  $N_{int} > 128$ , and  $N_{sb, tb} > 64$ . ■

**Remark 2.4.** We address the following inverse problem: suppose that the boundary conditions in equations (2) and (2.21), which may also include initial conditions, are unknown. This could render the forward problem associated with the PDE ill-posed, meaning a unique solution might not be guaranteed. However, we assume noiseless measurements of the underlying solution  $I$  are available within a subdomain  $D' \subset D$ . In most cases, PINNs achieve minimal errors with training times of less than one minute. Due to their simplicity and efficiency, PINNs provide an attractive alternative to current data assimilation methods, particularly in high-dimensional problems. ■

The error estimate primarily relates the overall generalization error to the training error. It uses the stability of the PDE to establish an upper bound based on the PDE residual, which is influenced by both training and quadrature errors. As long as the training errors remain independent of the underlying dimensionality, the above estimate implies that the PINNs described in Algorithms 2.1 and 2.2 will not be impacted by the curse of dimensionality.

### 3 Numerical experiments

The PINN algorithms 2.1 and 2.2 were implemented using the PyTorch framework [33]. All numerical experiments were performed on an Apple MacBook with an M3 chip and 24 GB of RAM. Several key hyperparameters are essential to the PINNs framework, including the quantity of hidden layers  $K - 1$ , layer width, selected activation function  $\sigma$ , parameter  $\lambda$  in the loss function, regularization parameter  $\lambda_{reg}$  in the cumulative loss, and the specific gradient descent optimization algorithm. For the activation function  $\sigma$ , we select the hyperbolic tangent (tanh), which ensures the smoothness properties required by theoretical guarantees for the neural networks are obtained. We employ the second-order LBFGS optimizer to improve convergence. For fine-tuning the remaining hyperparameters, we adopt the ensemble training method described in [2], [29], [30] and [31]. This method involves evaluating different values for the number of hidden layers, layer depth, parameter  $\lambda$ , and regularization term  $\lambda_{reg}$ , as illustrated in Table 1. Each hyperparameter set is used to retrain the model  $n_\theta$  times in parallel with different random weight initializations. The configuration yielding the lowest training loss is then selected as the best model.

### 3.1 Forward problem: data driven

#### 3.1.1 Radiation distribution of 1D infinite wall with Gaussian source

This model is based on a non-scattering medium situated between 1D infinite parallel black walls. The model contains Gaussian source term. We assume a constant extinction coefficient for the medium. The following radiative transfer equation describes this problem [24]:

$$\mu \frac{dI}{dx} + k_e I = \exp\left(-\frac{(x-c)^2}{\alpha^2}\right), \quad x, c \in [0, 1] \quad (3.1)$$

The boundary conditions are:

$$I(0, \mu) = k_e^{-1} \exp\left(-\frac{c^2}{\alpha^2}\right), \quad \mu > 0 \quad (3.2a)$$

$$I(1, \mu) = k_e^{-1} \exp\left(-\frac{(1-c)^2}{\alpha^2}\right), \quad \mu < 0 \quad (3.2b)$$

The analytical solution (for  $\mu > 0$ ) is provided as:

$$I(x, \mu) = I(0, \mu) \exp\left(-\frac{k_e x}{\mu}\right) - \frac{\alpha \sqrt{\pi}}{2\mu} \exp\left\{-\frac{k_e}{\mu} \left[x - \left(\frac{\alpha^2 k_e}{4\mu} + c\right)\right]\right\} \\ \times \left[ \operatorname{erf}\left(-\frac{k_e \alpha}{2\mu} + \frac{c-x}{\alpha}\right) - \operatorname{erf}\left(-\frac{k_e \alpha}{2\mu} + \frac{c}{\alpha}\right) \right]. \quad (3.3)$$

In this scenario,  $\alpha = 0.02$ ,  $c = 0.5$ , and  $\mu = 0.5$ . We compare the radiation intensity distributions calculated for

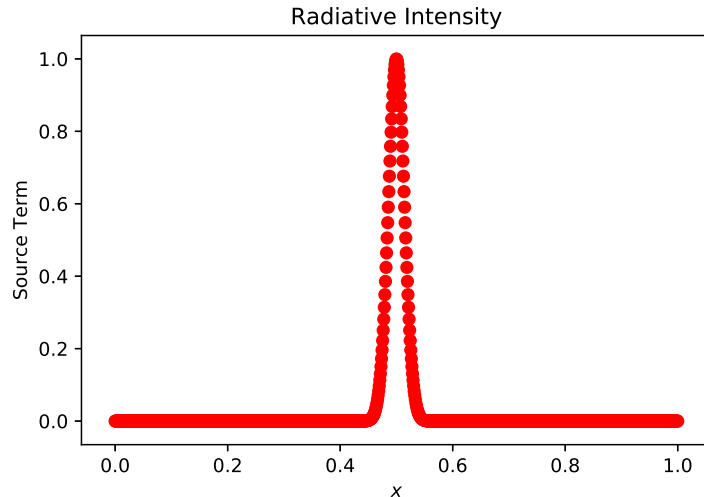


Figure 5: Source term of Eq.3.1.

the direction  $\mu = 0.5$  across media with varying extinction coefficients:  $k_e = 0.1$ ,  $k_e = 1$ , and  $k_e = 10 m^{-1}$ . Figure 5 represent the source term of the model. The predicted and exact solutions of the RTE for  $k_e = 0.1$ ,  $k_e = 1$ , and  $k_e = 10 m^{-1}$  are presented in Figures 6, 7, and 8, respectively.

The learned PINN solution are consistent and closely align with the exact solutions for all three scenarios. Table 2 demonstrates that the errors remain minimal, further highlighting the PINN's capability to accurately approximate the PDE with low computational cost. We have compared our result with some published works, including [51], [14], [27], and [48]. The authors simulated the model's relative error for parameters  $\mu = 0.5$ ,  $\alpha = 0.02$ , and  $c = 0.5$ . For the meshfree method by Zhao et al. [51], the relative error at  $k_e = 0.1, 1$ , and  $10 m^{-1}$ , with meshes ranging from 10 to 400, decreases from 21.77 to  $1.95 \times 10^{-3}$ , 6.35 to  $0.36 \times 10^{-2}$ , and 2.29 to  $0.49 \times 10^{-2}$ , respectively. For the DFEM [14], the relative error at  $k_e = 0.1, 1$ , and  $10 m^{-1}$ , with meshes ranging from 10 to 400, reduces from 1.95 to  $3.49 \times 10^{-4}$ , 2.05 to  $5.09 \times 10^{-4}$ , and 1.74 to  $0.15 \times 10^{-2}$ , respectively. For the generalized lattice Boltzmann method, with meshes between 20 and 200, the relative error at  $k_e = 0.1, 1$ , and  $10 m^{-1}$  decreases from  $1.6 \times 10^{-2}$  to  $8.9 \times 10^{-5}$ ,  $7.4 \times 10^{-2}$  to  $5.3 \times 10^{-4}$ , and 1.86 to  $0.32 \times 10^{-4}$ , respectively. In contrast, the PINN method achieves a relative  $L^2$  error of  $6.4 \times 10^{-4}$  at  $k_e = 10 m^{-1}$ .

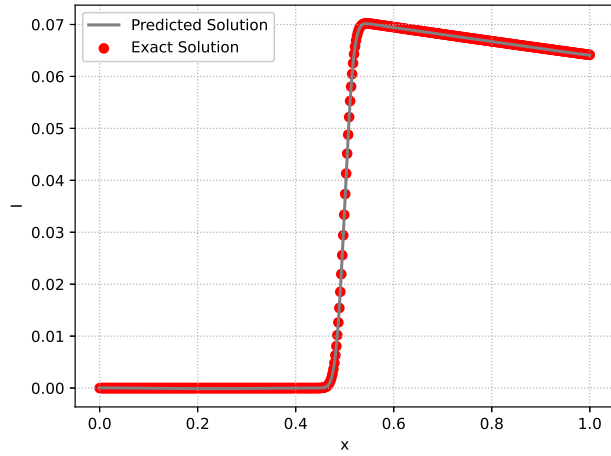


Figure 6: Radiation distribution with a Gaussian source at an extinction coefficient  $k_e = 0.1m^{-1}$ .

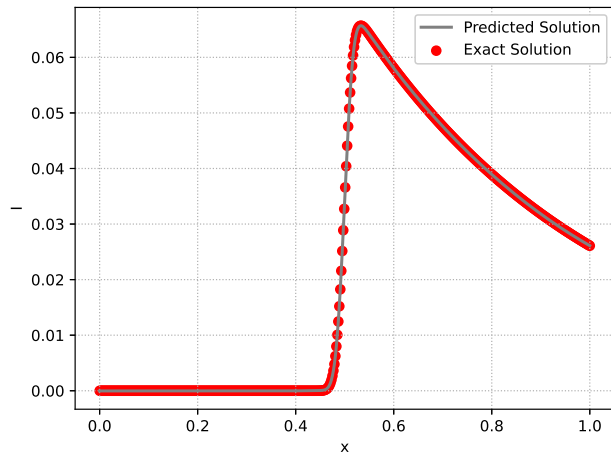


Figure 7: Radiation distribution with a Gaussian source at an extinction coefficient  $k_e = 1m^{-1}$ .

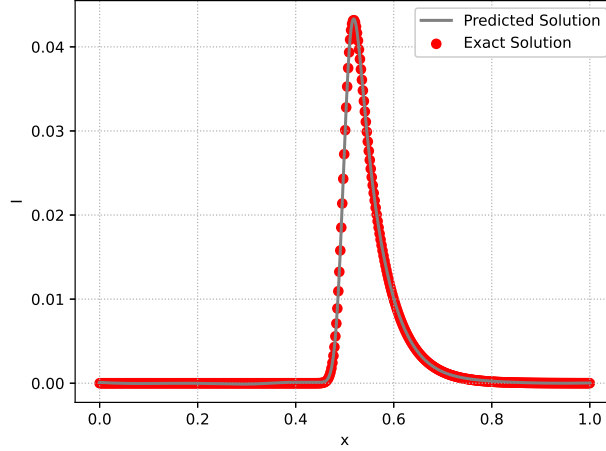


Figure 8: Radiation distribution with a Gaussian source at an extinction coefficients  $k_e = 10m^{-1}$ .

Case	$N_{\text{int}}$	$N_{\text{sb}}$	$K - 1$	$\bar{d}$	$\lambda$	$E_T$	$\ I - I^*\ _{L^2}$	Training Time (sec.)
1	8192	4096	4	20	0.1	0.0001	4.24e-05	23
2	8192	4096	4	20	1	0.0002	3.77e-05	16
3	8192	4096	4	20	0.1	0.0008	4.09e-05	30

Table 2: Results for the 1D infinite wall with a Gaussian source term.

### 3.1.2 Infinite wall with discontinuous source term

In this section, we have presented a new model for the radiation transfer equation in graded-index media. There are several types of deficiencies that arise with traditional methods like the LSFEM and generalized GFEM, as noted in [50]. This model investigates the transfer of heat through radiation in an infinite slab with discontinuous source term. For this scenario, the exact analytical solution is provided as

$$I(x, \mu) = \mathbf{1}_{(x-0.5L)} \exp(-k_e(x-0.5L)) + \mathbf{1}_{(0.5L-x)}. \quad (3.4)$$

In this equation, the constant parameter  $k_e$  indicates the strength of extinction, while  $L$  represents the thickness of the slab. The unit step function is denoted by  $\mathbf{1}_{[\cdot]}$ . The medium is homogeneous, and the walls are considered black. The distribution of intensity,  $I(x, \mu)$ , is aligned in the  $\mu = 1$  direction, with  $L$  equal to 10. The term can easily derive from exact solution.

The radiation intensity distributions solved for the direction  $\mu = 1$  and  $L = 10$  are compared across media with varying extinction coefficients:  $k_e = 0.1m^{-1}$ ,  $k_e = 1m^{-1}$ ,  $k_e = 2m^{-1}$ , and  $k_e = 10m^{-1}$ . The boundary conditions for walls are set with unity. The predicted and exact solutions of the RTE are illustrated in Figures 9, 10, 11, and 12 for  $k_e = 0.1m^{-1}$ ,  $k_e = 1m^{-1}$ ,  $k_e = 2m^{-1}$ , and  $k_e = 10m^{-1}$ , respectively. The results obtained from the PINN demonstrate stability and show good agreement with the exact solutions across all four scenarios. Table 3 shows that errors remain low at both boundaries, demonstrating the PINN's capability to accurately approximate the PDE with minimal computational effort.

Case	$N_{\text{int}}$	$N_{\text{sb}}$	$K - 1$	$\bar{d}$	$\lambda$	$E_T$	$\ I - I^*\ _{L^2}$	Training Time (sec.)
1	8192	4096	8	24	0.1	0.0005	0.00010	22
2	8192	4096	8	24	0.1	0.0012	0.0004	18
3	8192	4096	8	24	0.1	0.0020	0.0005	19
4	8192	4096	8	24	1	0.009	0.0009	26

Table 3: Results for the radiation transport equation with an infinite wall with discontinuous source.

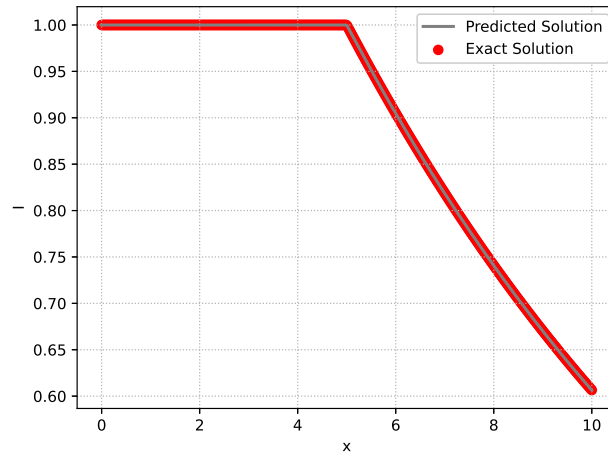


Figure 9: Radiation intensity distributions for an infinite wall with a discontinuous source, comparing results from the exact solution and the PINN method at  $k_e = 0.1m^{-1}$ .

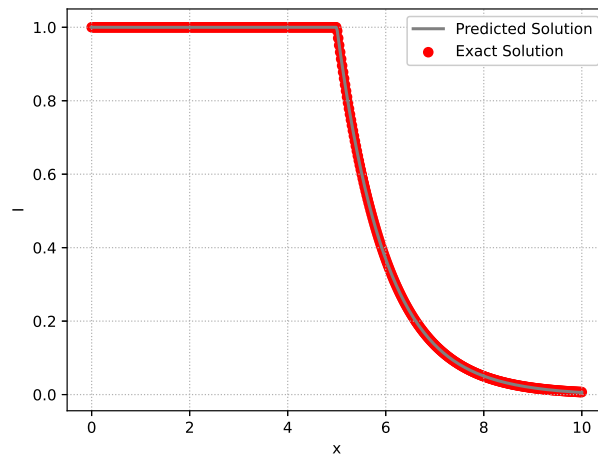


Figure 10: Radiation intensity distributions for an infinite wall with a discontinuous source, comparing results from the exact solution and the PINN method at an extinction coefficient of  $k_e = 1m^{-1}$ .

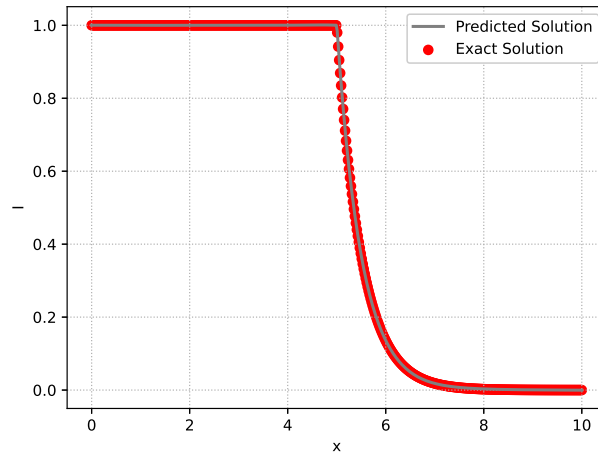


Figure 11: Radiation intensity distributions for an infinite wall with a discontinuous source, comparing results from the exact solution and the PINN method at an extinction coefficient of  $k_e = 2m^{-1}$ .

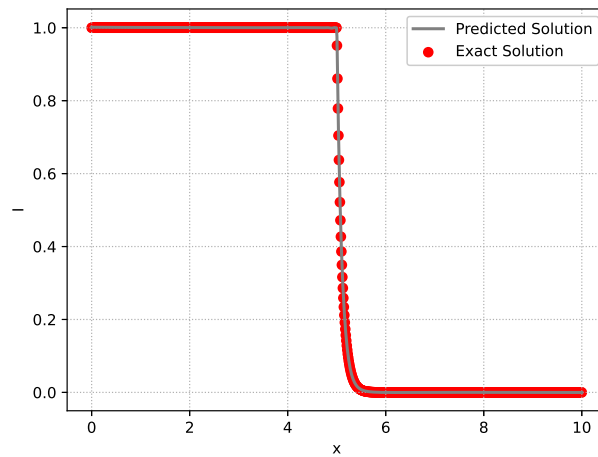


Figure 12: Radiation intensity distributions for an infinite wall with a discontinuous source, comparing results from the exact solution and the PINN method at an extinction coefficient of  $k_e = 10m^{-1}$ .



### 3.1.3 Square enclosure radiative distribution with discontinuous source along the diagonal

In this section, we have presented a new model for the radiation transfer equation in square enclosure. A 2D RTE problem is analyzed in this scenario. Figure 13 shows the layout of the square medium. An exact solution exists for this configuration is

$$I(x, y, \mu) = \mathbf{1}_{(x+y-L)} \exp\left[-k_e \frac{x+y-L}{\sqrt{2}}\right] + \mathbf{1}_{(L-x-y)}, \quad x, y \in [0, L]^2 \quad (3.5)$$

In this equation,  $k_e$  denotes the extinction strength,  $\mathbf{1}_{[\cdot]}$  represents the unit step function. Let the direction  $\Omega$  be  $\left[\frac{1}{\sqrt{2}}, \frac{1}{\sqrt{2}}\right]$  for an enclosure with a side length of  $L = 1$ . The left and bottom walls have boundary conditions with an intensity of one. Figures 14, 15, and 16 present the predicted and exact solutions of the RTE for  $k_e = 1m^{-1}$ ,  $k_e = 5m^{-1}$ , and  $k_e = 10m^{-1}$ , respectively. As illustrated in Table 4, the errors remain negligible at both boundaries, further showcasing the PINN's ability to accurately model the PDE while maintaining low computational expenses. We also present 3D plots in Figures 17, 18, and 19, which display the exact and predicted solutions of the RTE for  $k_e = 1m^{-1}$ ,  $k_e = 5m^{-1}$ , and  $k_e = 10m^{-1}$ , respectively.

Case	$N_{\text{int}}$	$N_{\text{sb}}$	$K - 1$	$\bar{d}$	$\lambda$	$E_T$	$\ I - I^*\ _{L^2}$	Training Time (sec.)
1	8192	4096	8	28	1	0.007	0.00056	18
2	8192	4096	8	28	1	0.0098	0.00048	19
3	8192	4096	8	28	1	0.020	0.00059	20

Table 4: Results for square medium radiative transfer along the diagonal.

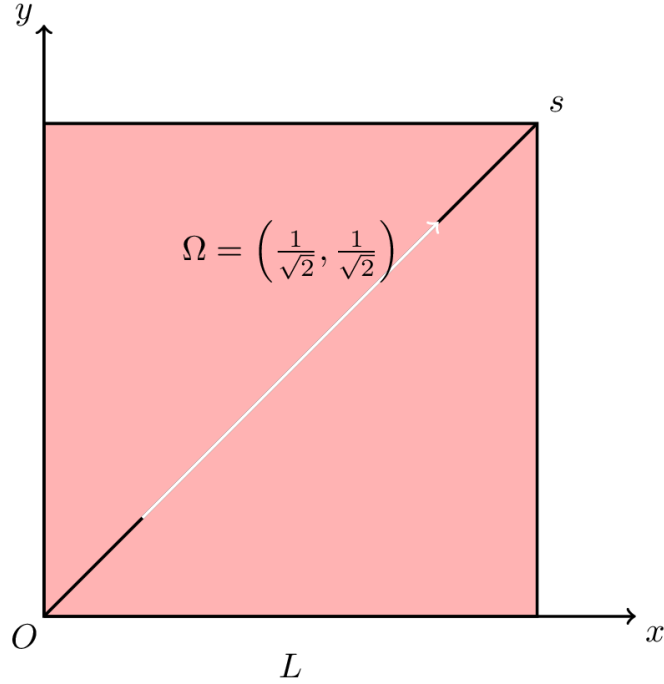


Figure 13: Schematic of the square solution domain.

### 3.1.4 Radiation distribution with a Gaussian source field along diagonal

This model is based on absorbing-emitting square enclosure. This test represents the 2D form of Eq. (3.1). The radiation transport equation can be modeled as

$$\mu \frac{dI}{dx} + \eta \frac{dI}{dy} + k_e I = \exp\left(-\frac{\left(\frac{x+y}{\sqrt{2}} - c\right)^2}{\alpha^2}\right), \quad x, y \in [0, 1] \quad (3.6)$$

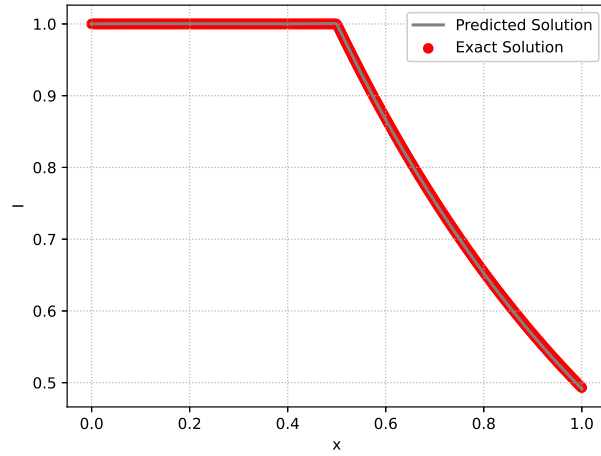


Figure 14: Radiation distribution along the diagonal at extinction coefficients  $k_e = 1m^{-1}$ .

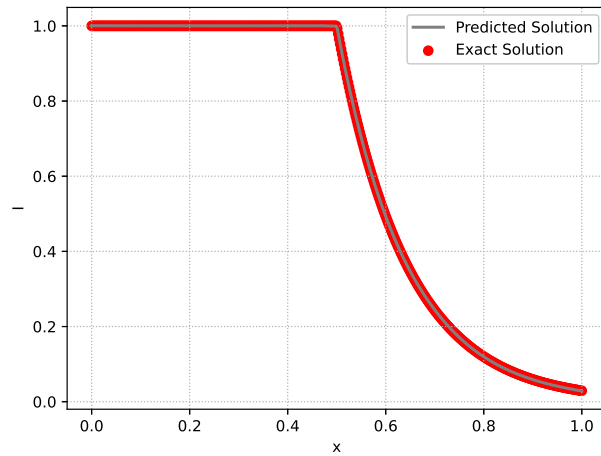


Figure 15: Radiation distribution along the diagonal at extinction coefficients  $k_e = 5m^{-1}$ .

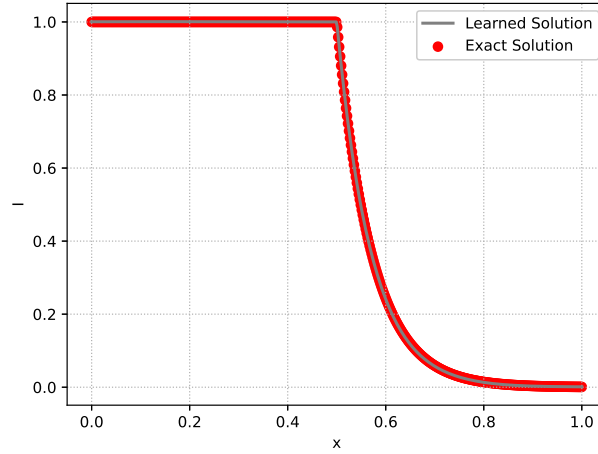


Figure 16: Radiation distribution along the diagonal at extinction coefficients  $k_e = 10m^{-1}$ .

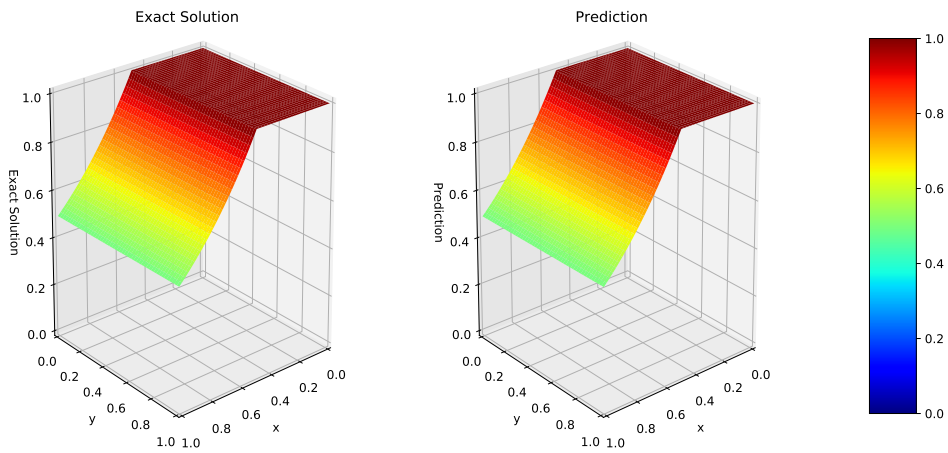


Figure 17: 3D plot for radiation distribution along the diagonal at extinction coefficients  $k_e = 1m^{-1}$ .

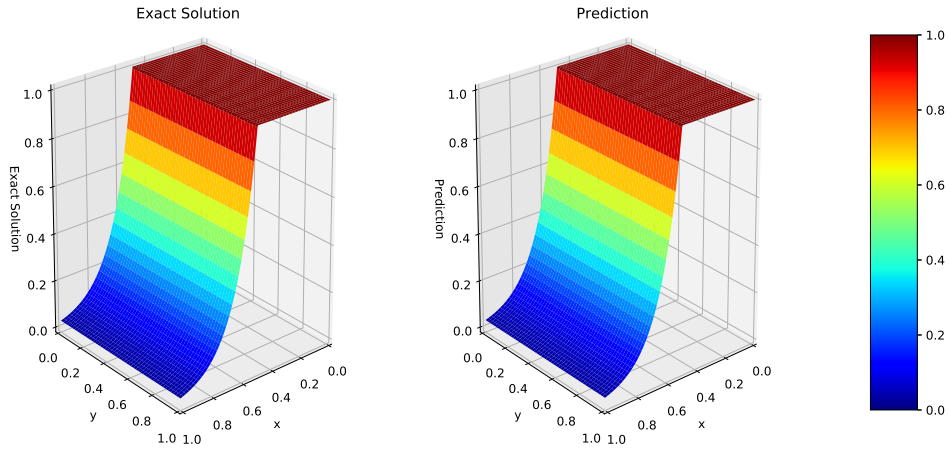


Figure 18: 3D plot for radiation distribution along the diagonal at extinction coefficients  $k_e = 5m^{-1}$ .

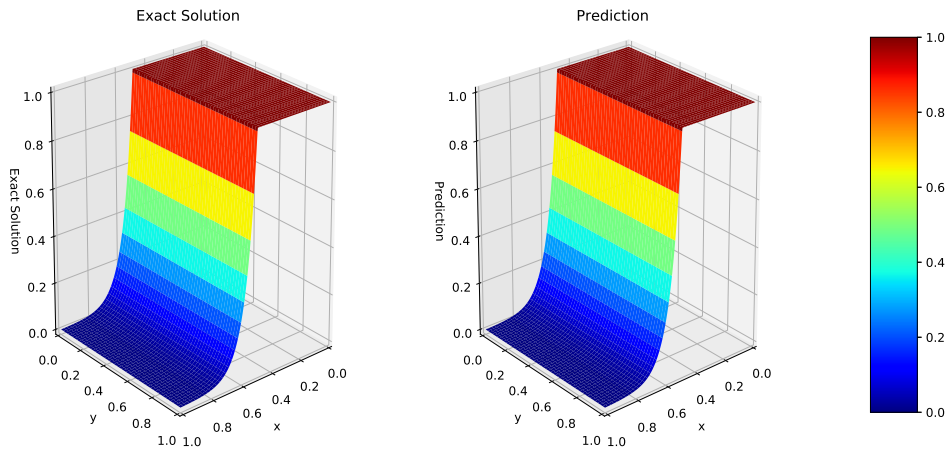


Figure 19: 3D plot for radiation distribution along the diagonal at extinction coefficients  $k_e = 10m^{-1}$ .

Let the incident direction be defined as  $\mu = \frac{\sqrt{2}}{2}$ ,  $\eta = \frac{\sqrt{2}}{2}$  and  $c = \frac{\sqrt{2}}{2}$ . The analytical solution [51] is

$$I(x, y) = \frac{\alpha\sqrt{\pi}}{2} \exp \left\{ -k_e \left[ \frac{|x+y|-|x-y|}{\sqrt{2}} - \frac{1-|x-y|}{\sqrt{2}} - \frac{\alpha^2 k_e}{4} \right] \right\} \times \left[ \operatorname{erf} \left( \frac{\alpha k_e}{2} + \frac{1-|x-y|}{\sqrt{2}\alpha} \right) - \operatorname{erf} \left( \frac{\alpha k_e}{2} + \frac{\frac{|x+y|-|x-y|}{\sqrt{2}} - \frac{1-|x-y|}{\sqrt{2}}}{\alpha} \right) \right] \quad (3.7)$$

Under the conditions  $x = y$  with black and cold boundary conditions [14], we utilized a PINN to determine the radiation distribution along the square enclosure's diagonal (where  $y = x$ ). Figure 20 represents the source term. Figures 21, 22, and 23 illustrate exact and predicted solutions of the RTE for  $k_e = 0.1m^{-1}$ ,  $k_e = 1m^{-1}$ , and  $k_e = 2m^{-1}$ , respectively. The errors, as shown in Table 5, are minimal at both boundaries, further demonstrating the PINN's capability to accurately approximate the PDE with low computational cost.

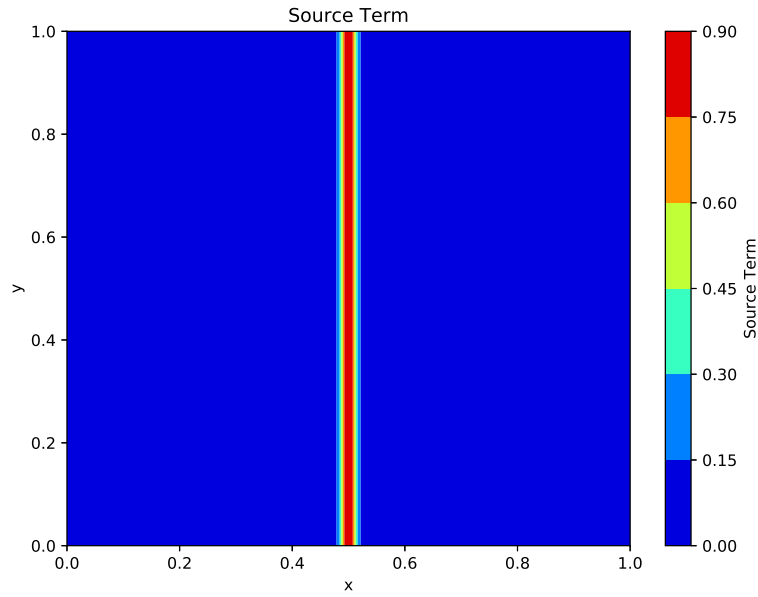


Figure 20: Source term at  $x = y$ .

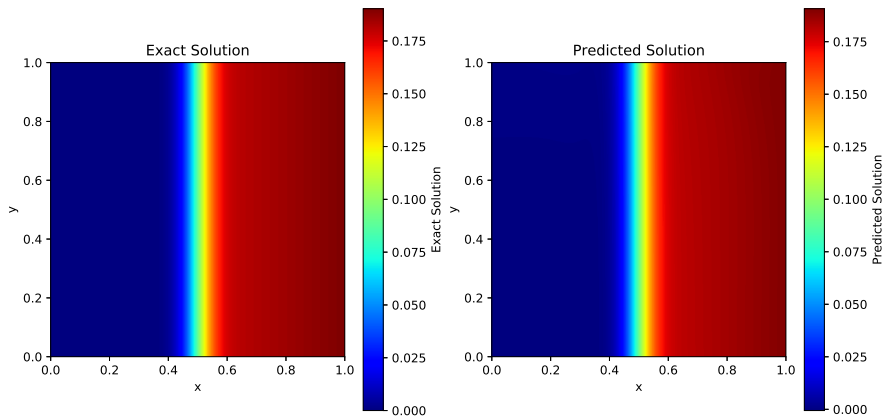


Figure 21: Radiation distribution with a Gaussian source, solved by PINN and exact at  $k_e = 0.1m^{-1}$  for  $x = y$ .

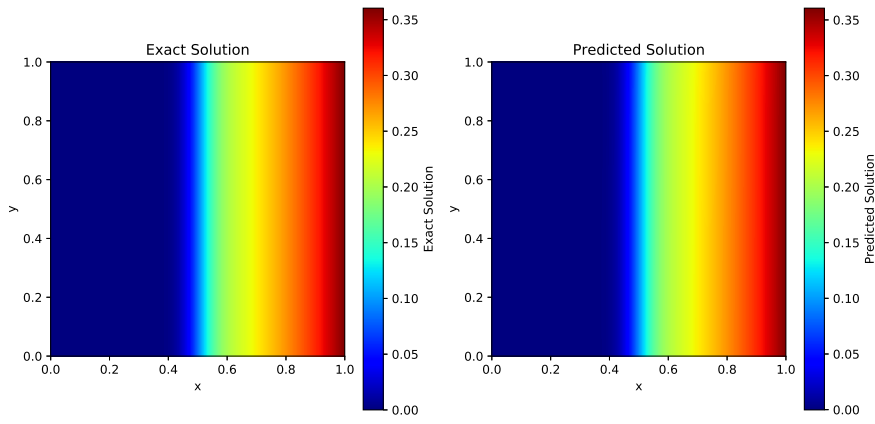


Figure 22: Radiation distribution with a Gaussian source, solved by PINN and exact at  $k_e = 1m^{-1}$  for  $x = y$ .

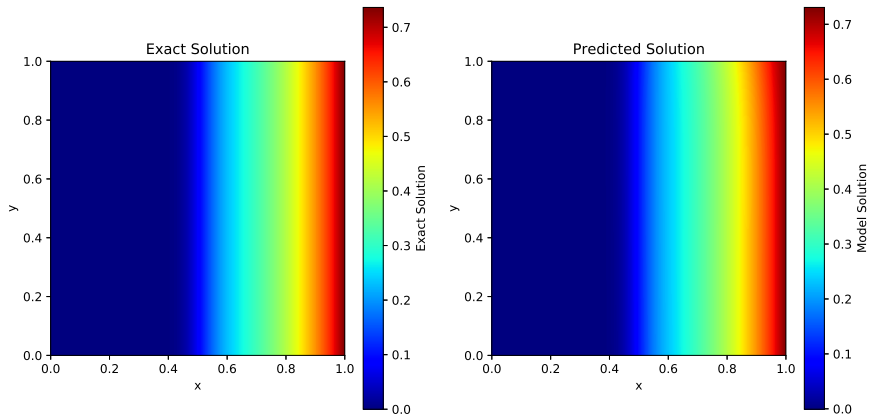


Figure 23: Radiation distribution with a Gaussian source, solved by PINN and exact at  $k_e = 2m^{-1}$  for  $x = y$ .

Case	$N_{\text{int}}$	$N_{\text{sb}}$	$K - 1$	$\bar{d}$	$\lambda$	$E_T$	$\ I - I^*\ _{L^1}$	Training Time (sec.)
1	8192	4096	4	20	0.1	0.00029	0.0002	9
2	8192	4096	4	20	0.1	0.0008	0.0012	10
3	8192	4096	4	20	0.1	0.0002	0.003	17

Table 5: Results of the radiation transport equation for Gaussian-shaped emissive field along the diagonal.

### 3.1.5 2D radiation distribution with Gaussian source term

Assume  $x \neq y$  in Eq.(3.6). Fig. 24 illustrates the source term in Eq.(3.6). Figs. 25, and 26 depict both the exact and predicted solutions of the RTE for  $k_e = 0.1m^{-1}$  and  $k_e = 1m^{-1}$  respectively. The errors, as presented in Table 6, are minimal, further highlighting the ability of the PINN with minimal computational effort accurately. At  $k_e = 1m^{-1}$ , the relative average error of the meshfree method [51] is 0.7. The relative error of the MRT lattice Boltzmann method [15] at  $k_e = 1m^{-1}$  is 2.5%. [47] simulated the same model using the lattice Boltzmann method and compared the results with the GFEM. Both [47] and [51] showed that for small values of  $k_e$ , the GFEM and the meshfree method, respectively, performed poorly.

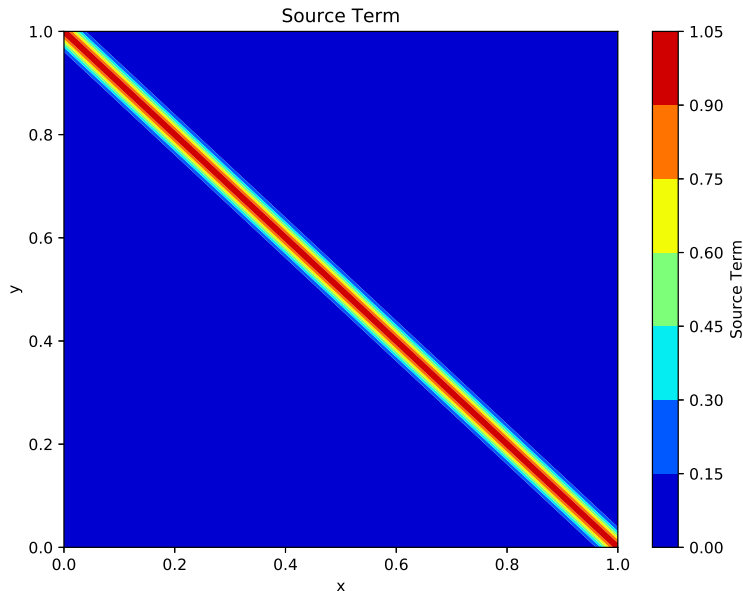


Figure 24: Source term at  $x$  is not equal to  $y$ .

Case	$N_{\text{int}}$	$N_{\text{sb}}$	$K - 1$	$\bar{d}$	$\lambda$	$E_T$	$\ I - I^*\ _{L^1}$	Training Time (sec)
1	8192	4096	4	20	0.1	0.0008	0.04	31
2	8192	4096	4	20	0.1	0.0009	0.05	27

Table 6: Results for 2D Radiation distribution with a Gaussian source(forward).

## 3.2 Inverse problems

### 3.2.1 2D radiation distribution with Gaussian source term

The numerical experiment of section (3.1.5) is performed as an inverse problem using Algorithm 2.2. In this experiment, we excluded the boundary conditions. Figs.27 and 28 show the exact and predicted solutions of the RTE for  $k_e = 0.1m^{-1}$  and  $k_e = 1m^{-1}$ , respectively. The errors, shown in Table 7, are minimal for different  $k_e$  values, demonstrating that the PINN is with high accuracy and at a meager computational cost. At  $k_e = 1m^{-1}$ , the relative average error of the mass-free method [51] is 0.7. At  $k_e = 1m^{-1}$ , the relative error of the MRT lattice

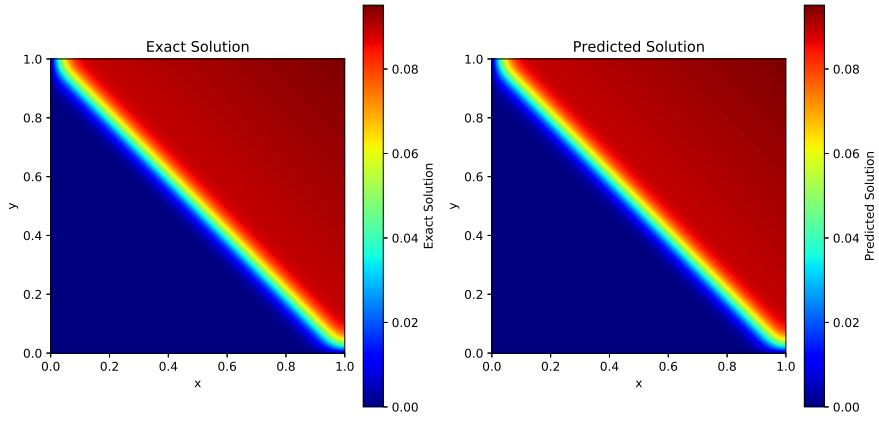


Figure 25: 2D Radiation distribution with a Gaussian source, solved by PINN and exact at  $k_e = 0.1m^{-1}$ .

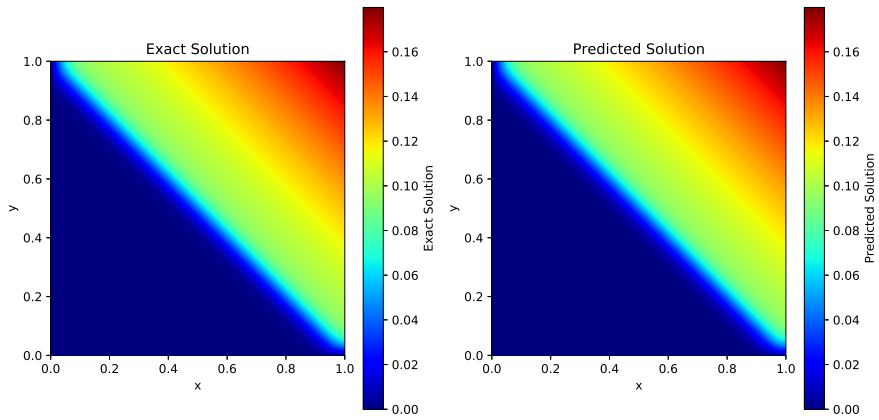


Figure 26: 2D Radiation distribution with a Gaussian source, solved by PINN and exact at  $k_e = 1m^{-1}$ .



Boltzmann algorithm, as simulated by Feng et al. [15], is 2.5%. The PINN method demonstrates a relative error of 0.9% at  $k_e = 1$ , notably lower than that of other methods.

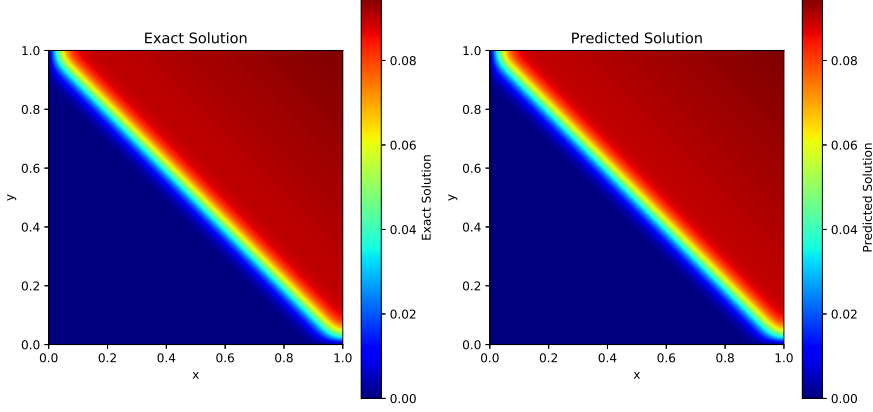


Figure 27: 2D Radiation distribution with a Gaussian source, solved by inverse PINN and exact at  $k_e = 0.1m^{-1}$ .

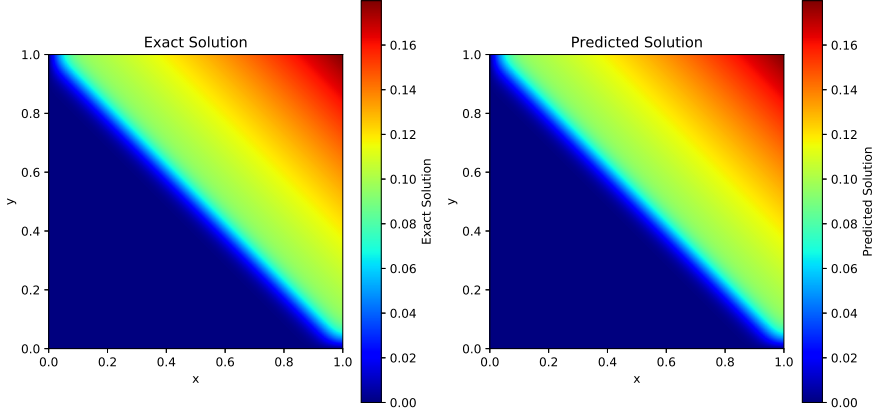


Figure 28: 2D Radiation distribution with a Gaussian source, solved by inverse PINN and exact at  $k_e = 1m^{-1}$ .

Case	$N_{\text{int}}$	$N_{\text{d}}$	$K - 1$	$\bar{d}$	$\lambda$	$E_T$	$\ I - I^*\ _{L^1}$	Training Time (sec.)
1	16384	8192	4	20	0.1	0.003	0.0008	36
2	16384	8192	4	20	0.1	0.003	0.0005	76

Table 7: Results for the 2D Radiation distribution with a Gaussian source(inverse).

## 4 Conclusion

Solving the RTE with graded index (2) presents a formidable challenge due to their inherent high-dimensional nature, especially when considering the most general scenario with seven dimensions. Furthermore, incorporating diverse physical phenomena such as emission, absorption, and scattering, alongside the variability in optical

parameters across the medium, adds complexity to devising efficient numerical algorithms. As highlighted earlier, existing methodologies often grapple with the curse of dimensionality, necessitating substantial computational resources to attain the desired level of precision. Hence, a critical need exists to engineer algorithms capable of simulating radiative transfer that balance ease of implementation, computational expediency, and accuracy. In our study, we propose an innovative solution to this challenge. Our approach, outlined in Algorithms 2.1 and 2.2, harnesses PINNs and sophisticated neural network architectures tailored specifically for approximating the radiative intensity outlined in the equation. Through iterative training using gradient descent, our network endeavors to minimize comprehensive loss function (2.15) and (2.16), respectively. This loss function encapsulates the residual error from integrating the neural network representation into the RTE (2). The residual errors are strategically positioned at training points, aligning with quadrature points based on a predefined quadrature rule. To alleviate the computational burden associated with high dimensionality, we employ Sobol low-discrepancy sequences as training points, optimizing efficiency while preserving accuracy.

Therefore, we posit that PINN algorithms 2.1 and 2.2 serve as a versatile, straightforward-to-implement, swift, and precise simulator for RTE phenomena. We demonstrate that this algorithm excels in speed and accuracy through numerical experiments. In essence, we contribute novel machine learning methodologies that offer a swift, user-friendly, and precise means of simulating various facets of radiation heat transfer in graded index phenomena. Our results showed that this approach worked well to reduce numerical errors, as there were no strange bumps in the results.

## Declaration of competing interest

The authors declare that they have no competing interests.

## Acknowledgment

The first author expresses sincere gratitude to his guide, Prof. S. Sundar, for his valuable suggestions and guidance throughout the preparation of this manuscript.

## Appendix

**Appendix D.1.** Assume  $I \in L^2(\mathbf{D})$  is the unique weak solution to the RTE in graded-index media, where the coefficients  $0 \leq k_e, k_s \in L^\infty(D \times S)$ , and phase function  $\Phi(\boldsymbol{\Omega}, \boldsymbol{\Omega}', \xi, \xi') \in C^p(S \times \Pi \times S \times \Pi)$  for some  $p > 0$ . Let  $I^* = I_\Theta \in C^p(\mathbf{D})$  be the solution generated by Algorithm 2.1 (forward PINN applied to the equation). Assume the condition  $\max\{HK_V(I^*), HK_V(R_{int, \Theta^*})\} < \infty$ , where  $HK_V$  represents the Hardy-Krause variation. Further, assume that Sobol points are used as training points  $\zeta_{int}, \zeta_{sb}, \zeta_{tb}$ , and a Gauss-quadrature rule of order  $a = a(p)$  is applied to approximate the scattering term in residual. Additionally, we assume that the functions  $f(s, \boldsymbol{\Omega}) \in D \times S$  arbitrary chosen in a manner consistent with the general model structure of the radiative transport equation. Under these assumptions:

$$n^2 k_a I_b(T_g) \leq n^2 k_a I(T_g) + f(s, \boldsymbol{\Omega}),$$

$$\frac{1}{n \sin \theta} \frac{\partial}{\partial \varphi} ((s_1 \cdot \nabla n)I) + \frac{1}{n \sin \theta} \frac{\partial}{\partial \theta} (I(\boldsymbol{\Omega} \cos \theta - k) \cdot \nabla n) \leq M\bar{I}, \quad M > 0.$$

The estimation of the generalized error for the forward problem is

$$(E_G)^2 \leq V \left( (E_T^{tb})^2 + \nu (E_T^{sb})^2 + \nu (E_T^{int})^2 \right) + VV_2 \left( \frac{(\log(N_{tb}))^{2d}}{N_{tb}} + \nu \frac{(\log(N_{sb}))^{2d}}{N_{sb}} + \nu \frac{(\log(N_{int}))^{2d+1}}{N_{int}} + \nu N_S^{-2a} \right), \quad (4.1)$$

where:

$$\begin{aligned} \bar{V} &= (\|\mathbf{D}\|, \|\Phi\|_{C^p}, \|\hat{I}\|), \\ V &= \left( T + \nu V_1 \bar{T}^2 \exp(\nu V_1 T) \right), \\ V_1 &= \frac{2\nu(\|k_s\|_{L^\infty} + \|\Sigma_g\|_{L^\infty})}{4\pi}, \\ V_2 &= \max\{HK_V(R_{tb}^*)^2, HK_V(R_{sb}^*)^2, HK_V(R_{int}^*)^2, \bar{V}\}. \end{aligned}$$

*Proof.* We are following [29]

$$\mathcal{E}(I^*, \Phi) = \sum_{i=1}^{N_S} w_i^S \Phi(\Omega, \Omega_i^S, \xi, \xi_i^S) I^*(t, s, \Omega_i^S, \xi_i^S) - \int_{4\pi} \Phi(\Omega, \Omega', \xi, \xi') I^*(t, s, \Omega, \xi) d\Omega', \quad (4.2)$$

$$\bar{I} = I^* - I,$$

$$\begin{aligned} \frac{n}{c_0} \frac{\partial}{\partial t} \bar{I} + (k_e + \Omega \cdot \nabla) \bar{I} + \frac{1}{n \sin \theta} \frac{\partial}{\partial \theta} \{ \bar{I} (\Omega \cos \theta - k) \cdot \nabla n \} + \frac{1}{n \sin \theta} \frac{\partial}{\partial \varphi} \{ (s_1 \cdot \nabla n) \bar{I} \} \\ = n^2 k_a \bar{I}_b(T_g) + \frac{k_s}{4\pi} \int_{4\pi} \Phi(\Omega, \Omega', \xi, \xi') \bar{I}(t, s, \Omega, \xi) d\Omega' + \mathcal{E}(I^*, \Phi), \end{aligned} \quad (4.3)$$

We define

$$\begin{aligned} \bar{I}(0, s, \Omega, \xi) &= R_{tb}^*, \quad (s, \Omega, \xi) \in D \times S \times \Pi \\ \bar{I}(t, s, \Omega, \xi) &= R_{sb}^*, \quad (t, s, \Omega, \xi) \in \beta \times \Pi \end{aligned} \quad (A)$$

Multiplying Eq.(4.3) by  $\bar{I}$  on both side,

$$\begin{aligned} \frac{n}{2c_0} \frac{d\bar{I}^2}{dt} = -k_e \bar{I}^2 - (\Omega \cdot \nabla_s) \left( \frac{\bar{I}^2}{2} \right) - \frac{1}{n \sin \theta} \frac{\partial}{\partial \theta} \{ \bar{I}^2 (\Omega \cos \theta - k) \cdot \nabla n \} - \frac{1}{n \sin \theta} \frac{\partial}{\partial \varphi} \{ (s_1 \cdot \nabla n) \bar{I}^2 \} \\ + n^2 k_a \bar{I}_b \bar{I}(T_g) - \frac{k_s}{4\pi} \int_{4\pi} \Phi(\Omega, \Omega', \xi, \xi') \bar{I}(t, s, \Omega, \xi) \bar{I}((t, s, \Omega', \xi) d\Omega' + \mathcal{E}(I^*, \Phi) \bar{I}. \end{aligned} \quad (4.4)$$

We can observe that  $\frac{1}{n \sin \theta} \frac{\partial}{\partial \varphi} \{ (s_1 \cdot \nabla n) \bar{I} \} + \frac{1}{n \sin \theta} \frac{\partial}{\partial \theta} \{ \bar{I} (\Omega \cos \theta - k) \cdot \nabla n \} \leq M \bar{I}$ ,  
 $n^2 k_a \bar{I}_b(T_g) \leq n^2 k_a \bar{I}(T_g) + f(s, \Omega)$ ,  
And

$$\int_{D \times S \times \Pi} |f(s, \Omega) \bar{I}| ds d\Omega \leq \int_{D \times S \times \Pi} |f|^2 ds d\Omega + \int_{D \times S \times \Pi} |\bar{I}|^2 ds d\Omega. \quad (4.5)$$

We substitute the values into Eq.(4.4), integrate the result over  $D \times S \times \Pi$ , and apply integration by parts and Cauchy sequence and  $k_e, k_s > 0$ , and  $t \in (0, T]$

$$\begin{aligned} \frac{n}{2c_0} \frac{d}{dt} \int_{D \times S \times \Pi} \bar{I}^2(t, s, \Omega, \xi) ds d\Omega \leq \int_{D \times S \times \Pi} \bar{I}^2(t, s, \Omega, \xi) ds d\Omega - \int_{(\partial D \times S \times \Pi)_-} (\Omega \cdot k(s)) \frac{\bar{I}^2(t, s, \Omega, \xi)}{2} dk(s) d\Omega \\ + \int_{D \times S \times \Pi} \frac{k_s}{4\pi} \int_{4\pi} \Phi(\Omega, \Omega', \xi, \xi') \bar{I}(t, s, \Omega, \xi) \bar{I}(t, s, \Omega', \xi') d\Omega' d\Omega ds \\ + \int_{D \times S \times \Pi} |f|^2 ds d\Omega + \int_{D \times S \times \Pi} \frac{(\mathcal{E}(I^*, \Phi)(t, s, \Omega, \xi))^2}{2} d\Omega ds. \end{aligned} \quad (4.6)$$

In this case,  $dk(s)$  signifies the surface measure on  $\partial D$ , and it can defined as

$$\beta = (\partial D \times S \times \Pi)_- = \{ (s, \xi, \Omega) \in \partial D \times S \times \Pi : \Omega \cdot k(s) \leq 0 \},$$

And with  $k(s)$  unit normal at  $s \in \partial D$ . Select a  $\hat{T} \in (0, T]$  and integrate Eq.(4.6) over  $(0, \hat{T})$ ,

$$\begin{aligned} \int_{D \times S \times \Pi} \bar{I}^2(\hat{T}, s, \Omega, \xi) ds d\Omega \leq \int_{D \times S \times \Pi} \bar{I}^2(0, s, \Omega, \xi) ds d\Omega + 2\nu \int_0^{\hat{T}} \int_{D \times S \times \Pi} \bar{I}^2(t, s, \Omega, \xi) dt ds d\Omega \\ + \nu \int_{\beta} |\Omega \cdot k| \bar{I}^2(t, s, \Omega, \xi) dt dk(s) d\Omega + U + \int_{D \times S \times \Pi} |f|^2 d\Omega ds + \nu \int_D \frac{(\mathcal{E}(I^*, \Phi))^2}{2} dX. \end{aligned} \quad (4.7)$$

Let

$$U = 2\nu \int_0^{\hat{T}} \int_{D \times S \times \Pi} \frac{k_s}{4\pi} \int_{4\pi} \Phi(\Omega, \Omega', \xi, \xi') \bar{I}(t, s, \Omega, \xi) \bar{I}(t, s, \Omega', \xi') d\Omega' d\Omega ds dt. \quad (4.8)$$

The value of  $U$  in Eq.(4.7) can be determined through repeated application of the Cauchy-Schwartz inequality as follows:

$$\begin{aligned} U &\leq 2\nu \int_0^{\bar{T}} \int_{D \times S \times \Pi} \bar{I}^2(t, s, \mathbf{\Omega}, \xi) d\Omega d\Omega' ds dt = \frac{2\nu(\|k_s\|_{L^\infty} + \|\Sigma_g\|_{L^\infty})}{4\pi} \int_0^{\bar{T}} \int_{D \times S \times \Pi} \bar{I}^2(t, s, \mathbf{\Omega}, \xi) d\Omega d\Omega' ds dt \\ &= V_1 \int_0^{\bar{T}} \int_{D \times S \times \Pi} \bar{I}^2(t, s, \mathbf{\Omega}, \xi) d\Omega d\Omega' ds dt. \end{aligned} \quad (4.9)$$

We get after identifying the constant from

$$\begin{aligned} \int_{D \times S \times \Pi} \bar{I}^2(t, s, \mathbf{\Omega}, \xi) ds d\Omega &\leq \int_{D \times S \times \Pi} (R_{tb}^*)^2 ds d\Omega + \nu \int_{\beta} (R_{sb}^*)^2 dt dk(s) d\Omega \\ &\quad + c\|(R_{int}^*)\|_{L^2(D_T \times S \times \Pi)}^2 + \nu \int_{\mathbf{D}} (\mathcal{E}(I^*, \Phi))^2 dX + \nu V_1 \int_0^{\bar{T}} \int_{D \times S \times \Pi} \bar{I}^2(t, s, \mathbf{\Omega}, \xi) d\Omega d\Omega' ds dt, \end{aligned} \quad (4.10)$$

We apply the integral in Gronwall inequality form to Eq.(4.10) to obtain:

$$\begin{aligned} \int_{D \times S \times \Pi} \bar{I}^2(t, s, \mathbf{\Omega}, \xi) ds d\Omega &\leq \left(1 + \nu V_1 \bar{T}^2 \exp^{\nu V_1 \bar{T}}\right) \\ &\quad \times \left( \int_{D \times \Pi \times S} (R_{tb}^*)^2 ds d\Omega + \nu \int_{\beta} (R_{sb}^*)^2 dt dk(s) d\Omega \right) \\ &\quad + \left(1 + \nu V_1 \bar{T}^2 \exp^{\nu V_1 \bar{T}}\right) \\ &\quad \times \left( \nu \|(R_{int}^*)\|_{L^2(D_T \times S \times \Pi)}^2 + (\mathcal{E}(I^*, \Phi))^2 dX \right), \end{aligned} \quad (4.11)$$

Integrating Eq.(4.11) over  $(0, T)$

$$\begin{aligned} (E_G)^2 = \int_{\mathbf{D}} \bar{I}^2(t, s, \mathbf{\Omega}, \xi) ds d\Omega &\leq \left(T + \nu V_1 \bar{T}^2 \exp^{\nu V_1 \bar{T}}\right) \left( \int_{D \times S \times \Pi} (R_{tb}^*)^2 ds d\Omega + \nu \int_{\beta} (R_{sb}^*)^2 dt dk(s) d\Omega \right) \\ &\quad + \left(\bar{T} + \nu V_1 \bar{T}^2 \exp^{\nu V_1 \bar{T}}\right) \left( \nu \|(R_{int}^*)\|_{L^2(D_T \times S \times \Pi)}^2 + (\mathcal{E}(I^*, \Phi))^2 dX \right). \end{aligned} \quad (4.12)$$

The points used for training in  $\zeta$  are sobol quadrature points, therefore the training error  $E_T$  represents the quasi-Monte Carlo quadrature of the integral Eq.(4.12). Consequently, this aligns with the Koksma-Hlawaka inequality [6],

$$\int_{D \times \Pi \times S} (R_{tb}^*)^2 ds d\xi d\Omega \leq (E_T^{tb})^2 + HK_V (R_{tb}^*)^2 \frac{(\log(N_{tb}))^{2d}}{N_{tb}}, \quad (4.13)$$

Similarly

$$\int_{\beta} (R_{sb}^*)^2 dt dk(s) d\Omega \leq (E_T^{sb})^2 + HK_V ((R_{sb}^*)^2) \frac{(\log(N_{sb}))^{2d}}{N_{sb}}, \quad (4.14)$$

$$c\|(R_{int}^*)\|_{L^2(D_T \times S \times \Pi)}^2 \leq (E_T^{int})^2 + HK_V (R_{int}^*)^2 \frac{(\log(N_{int}))^{2d+1}}{N_{int}}, \quad (4.15)$$

In this context,  $(\Omega^{\mathbf{S}}, \xi^{\mathbf{S}})$  for  $1 \leq i \leq N_{\mathbf{S}}$  represent points and weights of the Gauss quadrature rule  $a = a(p)$  as

$$\int_{\mathbf{D}} (\mathcal{E}(I^*, \Phi))^2 dX \leq \bar{V} N_{\mathbf{S}}^{-2a} \quad (4.16)$$

where  $\bar{V} = (\|\mathbf{D}\|, \|\Phi\|_{C^p}, \|\hat{I}\|)$ .

□

**Appendix D.2.** Let  $I \in L^2(D \times S \times \Pi)$ . Consider that  $I$  is unique weak solution of the RTE Eq.(2.21) with coefficients  $k_e, k_s \in L^\infty(D \times S)$ , where  $0 \leq k_e, k_s$ , and the bounds  $\min(k_e), \max(k_e)$  and  $\min(k_s), \max(k_s)$  correspond to the lower and upper limits of these coefficients. The phase function  $\Phi(\mathbf{\Omega}, \mathbf{\Omega}', \xi, \xi')$  is assumed to lie in the space  $C^p(S \times \Pi \times S \times \Pi)$  for some  $p > 0$ . Let  $I^* = I_\Theta \in C^p(D \times S \times \Pi)$  represent the output of Algorithm 2.1, which addresses the forward problem for the RTE with a graded index medium. Suppose that both the Hardy-Krause variation  $V_{HK}(I^*)$  and  $V_{HK}(R_{int, \Theta^*})$  are finite, and that Sobol points  $\zeta_{int}, \zeta_{sb}$  are used as training points as previously defined. Furthermore, assume that a Gauss-quadrature rule of order  $a = a(p)$  is applied to approximate the scattering term in residual. Now, assume  $M > 0$  and that the following inequalities hold:

$$n^2 k_a I_b(T_g) \leq n^2 k_a I(T_g) + f(s, \mathbf{\Omega}),$$

and

$$\frac{1}{n \sin \theta} \frac{\partial}{\partial \varphi} \{(s_1 \cdot \nabla n) I\} + \frac{1}{n \sin \theta} \frac{\partial}{\partial \theta} \{I(\mathbf{\Omega} \cos \theta - k) \cdot \nabla n\} \leq M I.$$

Under the assumption  $l > 0$ :

$$\left( \min(k_e) + \min(M) - \min(k_s) - 1 \right) - \frac{2\nu(\max(k_s) + \|\Sigma_g\|_{L^\infty})}{4\pi} > l, \quad (4.17)$$

And the above inequalities for  $M > 0$ , the generalization error for forward problems is estimated by:

$$\begin{aligned} (E_{G_{steady_f}})^2 &\leq V \left( \nu(E_T^{sb})^2 + \nu(E_T^{int})^2 \right) \\ &\quad + V \left( \frac{(\log(N_{sb}))^{2d}}{N_{sb}} + \nu \frac{(\log(N_{int}))^{2d}}{N_{int}} + \nu N_S^{-2a} \right), \end{aligned} \quad (4.18)$$

Where  $\bar{V} = (\|\mathbf{D}\|, \|\Phi\|_{C^p}, \|\hat{l}\|)$ ,  $C^\varepsilon$  is a constant dependent on  $l$  And

$$V = \max \left( \frac{2}{l}, \frac{2}{l} V_{HK} (R_{sb}^*)^2, \frac{2C^\varepsilon}{l} (R_{int}^*)^2, \frac{2C^\varepsilon}{l} \bar{V} N_S^{-2a} \right).$$

*Proof.* We are following [29]

$$\mathcal{E}_{S_f}(I^*, \Phi) = \sum_{i=1}^{N_S} w_i^S \Phi(\mathbf{\Omega}, \mathbf{\Omega}_i^S, \xi, \xi_i^S) I^*(s, \mathbf{\Omega}_i^S, \xi_i^S) - \int_{4\pi} \Phi(\mathbf{\Omega}, \mathbf{\Omega}', \xi, \xi') I^*(s, \mathbf{\Omega}, \xi) d\Omega', \quad (4.19)$$

$\bar{I} = I^* - I$ ,

$$\begin{aligned} (k_e + \mathbf{\Omega} \cdot \nabla) \bar{I} + \frac{1}{n \sin \theta} \frac{\partial}{\partial \theta} \{\bar{I}(\mathbf{\Omega} \cos \theta - k) \cdot \nabla n\} + \frac{1}{n \sin \theta} \frac{\partial}{\partial \varphi} \{(s_1 \cdot \nabla n) \bar{I}\} \\ = n^2 k_a \bar{I}_b(T_g) + \frac{k_s}{4\pi} \int_{4\pi} \Phi(\mathbf{\Omega}, \mathbf{\Omega}', \xi, \xi') \bar{I}(s, \mathbf{\Omega}, \xi) \bar{I}(s, \mathbf{\Omega}', \xi) d\Omega' + \mathcal{E}_{S_f}(I^*, \Phi), \end{aligned} \quad (4.20)$$

$$\bar{I}(t, s, \mathbf{\Omega}, \xi) = R_{sb}^*, \quad (t, s, \mathbf{\Omega}, \xi) \in \beta_o \times \Pi, \quad (A)$$

Multiplying Eq.(4.20) by  $\bar{I}$  on both side.

$$\begin{aligned} k_e \bar{I}^2 + \frac{1}{n \sin \theta} \frac{\partial}{\partial \theta} \{\bar{I}(\mathbf{\Omega} \cos \theta - k) \cdot \nabla n\} - \frac{1}{n \sin \theta} \frac{\partial}{\partial \varphi} \{(s_1 \cdot \nabla n) \bar{I}\} \\ = -(\mathbf{\Omega} \cdot \nabla_s) \left( \frac{\bar{I}^2}{2} \right) + n^2 k_a \bar{I}_b(T_g) \bar{I} + \frac{k_s}{4\pi} \int_{4\pi} \Phi(\mathbf{\Omega}, \mathbf{\Omega}', \xi, \xi') \bar{I}(s, \mathbf{\Omega}, \xi) \bar{I}(s, \mathbf{\Omega}', \xi) d\Omega' + \mathcal{E}_{S_f}(I^*, \Phi) \bar{I}, \end{aligned} \quad (4.21)$$

We can observe that  $\frac{1}{n \sin \theta} \frac{\partial}{\partial \varphi} \{(s_1 \cdot \nabla n) \bar{I}\} + \frac{1}{n \sin \theta} \frac{\partial}{\partial \theta} \{\bar{I}(\mathbf{\Omega} \cos \theta - k) \cdot \nabla n\} \leq M \bar{I}$ , and  $n^2 k_a \bar{I}_b(T_g) \leq n^2 k_a \bar{I}(T_g) + f(s, \mathbf{\Omega})$ .

Using Cauchy inequality for  $k_e, k_s > 0$ ,

$$\begin{aligned}
\int_{D \times S \times \Pi} \bar{I}^2(s, \Omega, \xi) ds d\Omega &\leq - \int_{(\partial D \times S \times \Pi)_-} (\Omega \cdot k(x)) \frac{\bar{I}^2(s, \Omega, \xi)}{2} dk(s) d\Omega \\
&+ \int_{D \times S \times \Pi} \frac{k_s}{4\pi} \int_{4\pi} \Phi(\Omega, \Omega', \xi, \xi') \bar{I}(s, \Omega, \xi) \bar{I}(s, \Omega', \xi') d\Omega' d\Omega ds \\
&+ \int_{D \times S \times \Pi} n^2 k_a \bar{I}(T_g) \bar{I}(s, \Omega, \xi) d\Omega ds + \int_{D \times S \times \Pi} f(s, \Omega) \bar{I}(s, \Omega, \xi) d\Omega ds \\
&+ \int_{D \times S \times \Pi} (\mathcal{E}_{S_f}(I^*, \Phi) \bar{I}(s, \Omega, \xi)) d\Omega ds,
\end{aligned} \tag{4.22}$$

In this case,  $dk(s)$  signifies the surface measure on  $\partial D$ , and it can be defined as

$$\beta_o = (\partial D \times S \times \Pi)_- = \{(s, \xi, \Omega) \in \partial D \times \Pi \times S : \Omega \cdot k(s) \leq 0\}$$

and with  $k(s)$  unit normal at  $s \in \partial D$ ,

Let

$$U = 2\nu \int_{D \times S \times \Pi} \frac{k_s}{4\pi} \int_{4\pi} \Phi(\Omega, \Omega', \xi, \xi') \bar{I}(s, \Omega, \xi) \bar{I}(s, \Omega, \xi) d\Omega d\Omega' ds, \tag{4.23}$$

Now  $U$  in Eq.(4.22) can be estimated by successive application of Cauchy-Schwartz inequality as

$$\begin{aligned}
U &\leq 2\nu \int_{D \times S \times \Pi} \bar{I}^2(s, \Omega, \xi) d\Omega d\Omega' ds = \frac{2\nu(\|k_s\|_{L^\infty} + \|\Sigma_g\|_{L^\infty})}{4\pi} \int_{D \times S \times \Pi} \bar{I}^2(s, \Omega, \xi) d\Omega d\Omega' ds \\
&= V_1 \int_{D \times S \times \Pi} \bar{I}^2(s, \Omega, \xi) d\Omega d\Omega' ds,
\end{aligned} \tag{4.24}$$

Utilizing integration by parts, and applying the presumed limits on  $k_e, k_s$ , and  $M$ , we derive:

$$\begin{aligned}
\left( \min(k_e) + \min(M) - \min(k_s) - 1 \right) \int_{D \times S \times \Pi} \bar{I}^2(s, \Omega, \xi) ds d\Omega &\leq \nu \int_{\beta_o} (\mathbb{R}_{sb}^*)^2 dk(s) d\Omega \\
&+ \int_{D \times S \times \Pi} (\mathbb{R}_{int}^*) \bar{I} d\Omega ds + \nu \int_{D \times S \times \Pi} (\mathcal{E}_{S_f}(I^*, \Phi)) \bar{I} dX \\
&+ \nu V_1 \int_{D \times S \times \Pi} \bar{I}^2(s, \Omega, \xi) d\Omega d\Omega' ds,
\end{aligned} \tag{4.25}$$

Given assumption 4.17,  $\exists$  an  $\varepsilon > 0$  such that

$$\left( \min(k_e) + \min(M) - \min(k_s) - 1 \right) - \frac{2\nu(\max(k_s) + \|\Sigma_g\|_{L^\infty})}{4\pi} - 2\varepsilon > \frac{l}{2},$$

We apply the  $\varepsilon$ -version of Cauchy's inequality.

$$\int_{D \times S \times \Pi} \bar{I}^2(s, \Omega, \xi) ds d\Omega \leq \frac{2}{l} \int_{\beta_o} (\mathbb{R}_{sb}^*)^2 dk(s) d\Omega + \frac{2C^\varepsilon}{l} \int_{D \times S \times \Pi} (\mathbb{R}_{int}^*)^2 d\Omega + \mathcal{E}_{S_f}(I^*, \Phi)^2 dX. \tag{4.26}$$

□

## References

- [1] A. I. Arbab. On compton scattering in dielectric medium. *Optik*, 127(20):8536–8541, 2016.
- [2] G. Bai, U. Koley, S. Mishra, and R. Molinaro. Physics informed neural networks (pinns) for approximating nonlinear dispersive pdes. *J. Comp. Math.*, 39:816–847, 2021.
- [3] D. Baillis, R. Coquard, J. H. Randrianalisoa, L. A. Dombrovsky, and R. Viskanta. Thermal radiation properties of highly porous cellular foams. *Special Topics & Reviews in Porous Media: An International Journal*, 4(2), 2013.
- [4] A. R. Barron. Universal approximation bounds for superpositions of a sigmoidal function. *IEEE Transactions on Information theory*, 39(3):930–945, 1993.
- [5] C. Beck, S. Becker, P. Grohs, N. Jaafari, and A. Jentzen. Solving the kolmogorov pde by means of deep learning. *Journal of Scientific Computing*, 88:1–28, 2021.
- [6] R. E. Caflisch. Monte carlo and quasi-monte carlo methods. *Acta numerica*, 7:1–49, 1998.
- [7] G. Cybenko. Approximations by superpositions of a sigmoidal function. *Mathematics of Control, Signals and Systems*, 2:183–192, 1989.
- [8] T. De Ryck, A. D. Jagtap, and S. Mishra. Error estimates for physics-informed neural networks approximating the navier–stokes equations. *IMA Journal of Numerical Analysis*, 44(1):83–119, 2024.
- [9] T. De Ryck and S. Mishra. Error analysis for physics-informed neural networks (pinns) approximating kolmogorov pdes. *Advances in Computational Mathematics*, 48(6):79, 2022.
- [10] T. De Ryck, S. Mishra, and R. Molinaro. wpinns: Weak physics informed neural networks for approximating entropy solutions of hyperbolic conservation laws. *SIAM Journal on Numerical Analysis*, 62(2):811–841, 2024.
- [11] V. Dolean, A. Heinlein, S. Mishra, and B. Moseley. Finite basis physics-informed neural networks as a schwarz domain decomposition method. In *International Conference on Domain Decomposition Methods*, pages 165–172. Springer, 2022.
- [12] H. Ebrahimi, A. Zamaniyan, J. S. S. Mohammadzadeh, and A. A. Khalili. Zonal modeling of radiative heat transfer in industrial furnaces using simplified model for exchange area calculation. *Applied Mathematical Modelling*, 37(16-17):8004–8015, 2013.
- [13] R. Evans, J. Jumper, J. Kirkpatrick, L. Sifre, T. Green, C. Qin, A. Zidek, A. Nelson, A. Bridgland, H. Penedones, et al. De novo structure prediction with deeplearning based scoring. *Annu Rev Biochem*, 77(363-382):6, 2018.
- [14] Y.-Y. Feng and C.-H. Wang. Discontinuous finite element method with a local numerical flux scheme for radiative transfer with strong inhomogeneity. *International Journal of Heat and Mass Transfer*, 126:783–795, 2018.
- [15] Y.-Y. Feng and C.-H. Wang. On the performance of a mrt lattice boltzmann algorithm for transient radiative transfer problems. *International Communications in Heat and Mass Transfer*, 128:105628, 2021.
- [16] A. Fokou, R. Tapimo, G. L. Ymeli, R. Tchinda, and H. T. T. Kamdem. Radiation distribution in inhomogeneous atmosphere-ocean system by discrete spherical harmonics method. *Journal of Quantitative Spectroscopy and Radiative Transfer*, 270:107707, 2021.
- [17] I. Goodfellow. *Deep learning*. MIT press, 2016.
- [18] K. Hornik, M. Stinchcombe, and H. White. Multilayer feedforward networks are universal approximators. *Neural networks*, 2(5):359–366, 1989.
- [19] Q. A. Huhn, M. E. Tano, and J. C. Ragusa. Physics-informed neural network with fourier features for radiation transport in heterogeneous media. *Nuclear Science and Engineering*, 197(9):2484–2497, 2023.
- [20] A. D. Jagtap and G. E. Karniadakis. Extended physics-informed neural networks (xpinns): A generalized space-time domain decomposition based deep learning framework for nonlinear partial differential equations. *Communications in Computational Physics*, 28(5), 2020.
- [21] A. D. Jagtap, E. Kharazmi, and G. E. Karniadakis. Conservative physics-informed neural networks on discrete domains for conservation laws: Applications to forward and inverse problems. *Computer Methods in Applied Mechanics and Engineering*, 365:113028, 2020.
- [22] I. E. Lagaris, A. Likas, and D. I. Fotiadis. Artificial neural networks for solving ordinary and partial differential equations. *IEEE transactions on neural networks*, 9(5):987–1000, 1998.

- [23] E. W. Larsen, F. Malvagi, and G. Pomraning. One-dimensional models for neutral particle transport in ducts. *Nuclear science and engineering*, 93(1):13–30, 1986.
- [24] L. Liu. Finite volume method for radiation heat transfer in graded index medium. *Journal of Thermophysics and Heat Transfer*, 20(1):59–66, 2006.
- [25] L. Liu. Meshless local petrov-galerkin method for solving radiative transfer equation. *Journal of thermophysics and heat transfer*, 20(1):150–154, 2006.
- [26] L. Liu. Least-squares finite element method for radiation heat transfer in graded index medium. *Journal of Quantitative Spectroscopy and Radiative Transfer*, 103(3):536–544, 2007.
- [27] X. Liu, Y. Huang, C.-H. Wang, and K. Zhu. Solving steady and transient radiative transfer problems with strong inhomogeneity via a lattice boltzmann method. *International Journal of Heat and Mass Transfer*, 155:119714, 2020.
- [28] L. Lu, X. Meng, Z. Mao, and G. E. Karniadakis. Deepxde: A deep learning library for solving differential equations. *SIAM review*, 63(1):208–228, 2021.
- [29] S. Mishra and R. Molinaro. Physics informed neural networks for simulating radiative transfer. *Journal of Quantitative Spectroscopy and Radiative Transfer*, 270:107705, 2021.
- [30] S. Mishra and R. Molinaro. Estimates on the generalization error of physics-informed neural networks for approximating a class of inverse problems for pdes. *IMA Journal of Numerical Analysis*, 42(2):981–1022, 2022.
- [31] S. Mishra and R. Molinaro. Estimates on the generalization error of physics-informed neural networks for approximating pdes. *IMA Journal of Numerical Analysis*, 43(1):1–43, 2023.
- [32] B. Moseley, A. Markham, and T. Nissen-Meyer. Finite basis physics-informed neural networks (fbpinns): a scalable domain decomposition approach for solving differential equations. *Advances in Computational Mathematics*, 49(4):62, 2023.
- [33] A. Paszke, S. Gross, S. Chintala, G. Chanan, E. Yang, Z. DeVito, Z. Lin, A. Desmaison, L. Antiga, and A. Lerer. Automatic differentiation in pytorch. *NIPS Autodiff Workshop*, 2017.
- [34] T. Pichard, G. W. Alldredge, S. Brull, B. Dubroca, and M. Frank. An approximation of the m 2 closure: application to radiotherapy dose simulation. *Journal of Scientific Computing*, 71(1):71–108, 2017.
- [35] M. Raissi, P. Perdikaris, and G. E. Karniadakis. Physics-informed neural networks: A deep learning framework for solving forward and inverse problems involving nonlinear partial differential equations. *Journal of Computational physics*, 378:686–707, 2019.
- [36] J. H. Randrianalisoa, L. A. Dombrovsky, W. Lipiński, and V. Timchenko. Effects of short-pulsed laser radiation on transient heating of superficial human tissues. *International Journal of Heat and Mass Transfer*, 78:488–497, 2014.
- [37] R. Riganti and L. D. Negro. Auxiliary physics-informed neural networks for forward, inverse, and coupled radiative transfer problems. *Applied Physics Letters*, 123(17), 2023.
- [38] M. Sead, M. Frank, A. Klar, R. Pinnau, and G. Thömmes. Efficient numerical methods for radiation in gas turbines. *Journal of Computational and Applied Mathematics*, 170(1):217–239, 2004.
- [39] K. Shukla, A. D. Jagtap, and G. E. Karniadakis. Parallel physics-informed neural networks via domain decomposition. *Journal of Computational Physics*, 447:110683, 2021.
- [40] J. Stoer. R. bulirsch introduction to numerical analysis springer-verlag. *Texts in Applied Mathematics*, 12:30, 2002.
- [41] Y.-S. Sun and B.-W. Li. Chebyshev collocation spectral method for one-dimensional radiative heat transfer in graded index media. *International Journal of Thermal Sciences*, 48(4):691–698, 2009.
- [42] C.-A. Wang, H. Sadat, and V. Le Dez. Meshless method for solving multidimensional radiative transfer in graded index medium. *Applied Mathematical Modelling*, 36(11):5309–5319, 2012.
- [43] S. Wang, X. Yu, and P. Perdikaris. When and why pinns fail to train: A neural tangent kernel perspective. *Journal of Computational Physics*, 449:110768, 2022.
- [44] L.-Y. Wei, H. Qi, Z.-T. Niu, Y.-T. Ren, and L.-M. Ruan. Reverse monte carlo coupled with runge-kutta ray tracing method for radiative heat transfer in graded-index media. *Infrared Physics & Technology*, 99:5–13, 2019.
- [45] Y. Xie, Y. Wang, and Y. Ma. Boundary dependent physics-informed neural network for solving neutron transport equation. *Annals of Nuclear Energy*, 195:110181, 2024.



- [46] D. Yarotsky. Error bounds for approximations with deep relu networks. *Neural networks*, 94:103–114, 2017.
- [47] H.-L. Yi, F.-J. Yao, and H.-P. Tan. Lattice boltzmann model for a steady radiative transfer equation. *Physical Review E*, 94(2):023312, 2016.
- [48] G. L. Ymeli and C.-H. Wang. Generalized lattice boltzmann method for radiative transfer problem in slab and irregular graded-index media. *Physical Review E*, 107(1):015302, 2023.
- [49] J. Yu, L. Lu, X. Meng, and G. E. Karniadakis. Gradient-enhanced physics-informed neural networks for forward and inverse pde problems. *Computer Methods in Applied Mechanics and Engineering*, 393:114823, 2022.
- [50] J. Zhao, J. Tan, and L. Liu. A deficiency problem of the least squares finite element method for solving radiative transfer in strongly inhomogeneous media. *Journal of Quantitative Spectroscopy and Radiative Transfer*, 113(12):1488–1502, 2012.
- [51] J. Zhao, J. Tan, and L. Liu. A second order radiative transfer equation and its solution by meshless method with application to strongly inhomogeneous media. *Journal of Computational Physics*, 232(1):431–455, 2013.